Super-Resolution Land Cover Mapping with Indicator Geostatistics

Alexandre Boucher[1] and Phaedon C. Kyriakidis[2]

[1]Department of Geological and Environmental Sciences
Stanford University

[2]Department of Geography
University of California at Santa Barbara

Abstract

Many satellite images have a spatial resolution coarser than the extent of land cover patterns on the ground, leading to mixed pixels whose composite spectral response consists of responses from multiple land cover classes. Spectral unmixing procedures only determine the fractions of such classes within a coarse pixel without locating them in space. Super-resolution or sub-pixel mapping aims at providing a fine resolution map of class labels, one that displays realistic spatial structure (without artifact discontinuities) and reproduces the coarse resolution fractions. In this paper, existing approaches for super-resolution mapping are placed within an inverse problem framework, and a geostatistical method is proposed for generating alternative synthetic land cover maps at the fine (target) spatial resolution; these super-resolution realizations are consistent with all the information available.

Indicator coKriging is used to approximate the probability that a pixel at the fine spatial resolution belongs to a particular class, given the coarse resolution fractions and (if available) a sparse set of class labels at some informed fine pixels. Such Kriging-derived probabilities are used in sequential indicator simulation to generate synthetic maps of class labels at the fine resolution pixels. This non-iterative and fast simulation procedure yields alternative super-resolution land cover maps that reproduce: (i) the observed coarse fractions, (ii) the fine resolution class labels that might be available, and (iii) the prior structural information encapsulated in a set of indicator variogram models at the fine resolution. A case study is provided to illustrate the proposed methodology using Landsat TM data from SE China.

1 Introduction

Sensors with spatial resolution larger than the extent of classes on the ground yield mixed pixels, i.e., pixels whose spectral signature is a composite of signatures of different classes. Spectral unmixing is the procedure of determining the fractions of such classes that occupy any coarse pixel; see, for example, Richards and Jia (1999) or Tso and Mather (2001) for a survey of unmixing methods. Spectral unmixing, however, provides only class fractions without locating within any coarse pixel the constituent classes. That additional task lies in the realm of super-resolution mapping, also termed sub-pixel mapping, or downscaling; see, for example, Atkinson (2001).

In this paper, we view super-resolution mapping from an inverse problem perspective (Menke, 1989; Bertero and Boccacci, 1998; Tarantola, 2005): that of reconstructing a fine resolution map of class labels from a set of coarse class fractions. The forward problem of computing coarse fractions from a fine resolution map of class labels is trivial. The inverse problem, however, is under-determined, in that it has multiple plausible solutions: many fine resolution class maps can lead to an equally good reproduction of the available coarse fractions. In order to solve such an under-determined inverse problem, one needs to invoke prior information that will resolve the inherent ambiguity. This prior information should pertain to the fine (target) spatial resolution, so that it constrains the "space" of possible spatial patterns of classes that can occur at that resolution. In what follows, we will occasionally refer to this fine resolution prior information as a model of spatial structure, structural model, or structural information, which, in this work, can also be loosely regarded as pertaining to texture (Tso and Mather, 2001).

The most primitive form of spatial structure is the rather unrealistic assumption of classes randomly distributed at the fine spatial resolution. Another particular form of prior information is the assumption of maximum class auto-correlation at the target resolution, which underpins several approaches for super-resolution mapping (Atkinson et al., 1997; Verhoeye et al., 2001; Atkinson, 2001; Tatem et al., 2001; Mertens et al., 2003). This prior structural model might be appropriate when the extent of spatial patterns on the ground is much larger than that of the coarse pixel, a scenario termed H-resolution by Jupp et al. (1988). Such a model, however, is too rigid, in that it cannot be adapted to generic scenes.

Moving away from the rigid notion of maximum spatial auto-correlation, prior information has been specified implicitly or explicitly in the form of parametric indicator variogram models. Atkinson (2001) and Makido and Shortridge (2005) used an iterative class swapping procedure to generate super-resolution maps, whereby a parametric function of distance (e.g., exponential decay) was used as a proxy for a formal indicator variogram model to determine the benefit of changing a simulated class label at any particular pixel in each iteration. Tatem et al. (2002, 2003) explicitly used indicator variogram models as objective function components within an

iterative optimization framework. Prior information has also been specified in the form of interactions between predefined groups of pixels (cliques) linked to the parametric energy function of a Markov Random Field model (Tso and Mather, 2001; Kasetkasem et al., 2005). Alternatively, that prior information could be extracted from analog images, by computing directly without any parametrization the probability of occurrence of different spatial patterns, i.e., sets of class labels over groups of pixels (Strebelle, 2002). This latter approach to prior information specification can account for complex spatial patterns (e.g., meandering objects) that cannot be adequately characterized by two-point statistics, such as indicator variograms.

In this work, we assume knowledge of the coarse resolution fractions; we do not address how such fractions were derived from the original satellite reflectance values. Moreover, we assume that these fractions are exact measurements with no error or inherent uncertainty; the possibility of relaxing this assumption is not pursued here due to space limitations. In addition, and contrary to many existing approaches to super-resolution mapping, we also consider the case whereby the analyst has access to a typically small set of class labels at the fine resolution, possibly obtained via ground surveys. Such sparse, with respect to the abundant coarse fractions, fine resolution data provide information on the actual location of classes at the target resolution, and hence should be reproduced exactly in the final maps.

After a prior model of spatial structure has been specified, a probabilistic formulation of inverse problems seeks to determine the conditional probability distribution of the unknowns given the available data; that probability distribution encapsulates our uncertainty about the unknown attribute values given the current level of information (Tarantola, 2005). In the context of super-resolution mapping, this amounts to determining the multivariate or multi-pixel conditional probability of obtaining any particular spatial combination of class labels at the target resolution, given the abundant coarse fractions and possibly some sparsely sampled class labels at that target resolution. That conditional distribution is typically complex with multiple modes and may not be analytically tractable. Instead of determining a single summary measure from the conditional distribution, such as its mean or mode, that distribution is "explored" by generating multiple samples or realizations from it (Mosegaard and Tarantola, 1995; Sambridge and Mosegaard, 2002; Kaipio and Somersalo, 2004; Tarantola, 2005). In our setting, this amounts to generating alternative simulated super-resolution maps of class labels that are consistent with all the information available; that is, the prior structural model, the coarse fractions, and the fine class labels if available. These simulated super-resolution maps can then be used to determine the likelihood of occurrence of patterns of classes over various groups or templates of pixels, by calculating the frequency of occurrence of such class patterns over the realizations.

More importantly, by using these synthetic super-resolution maps as inputs to a process simulation model, e.g., in a wildfire propagation simulator, one can build a

probability distribution for the model outputs in a Monte Carlo framework (Bachmann and Allgöwer, 2002). By fixing other input variables to a nominal value or set of values, one could also assess via Monte Carlo simulation the sensitivity of that model to an uncertain land cover map; see Crosetto et al. (2001) for a discussion of uncertainty and sensitivity analysis techniques in a remote sensing context. In our case, that sensitivity would pertain to the lack of class labels at the appropriate model resolution.

One of the earliest approaches to super-resolution land cover mapping is that of Verhoeye et al. (2001), who proposed a deterministic solution based on linear programming. This approach, however, does not acknowledge the existence of multiple super-resolution maps due to multiple optima in the linear programming formulation. In general, most existing algorithms for super-resolution land cover mapping are iterative in nature, and (rightfully so) yield different such maps depending on the initial map used in the iteration procedure. Mertens et al. (2003) adopted the same objective function as Verhoeye et al. (2001), but used a genetic algorithm to search for plausible super-resolution maps. Tatem et al. (2001) trained a Hopfield neural network to optimize an initial super-resolution map (used for further iterations) with the simultaneous objectives of coarse fraction reproduction and spatial auto-correlation maximization; that method was successfully tested on an actual case study (Tatem et al., 2003). Mertens et al. (2004) used wavelets to account for the resolution difference between fine class labels and coarse fractions. At the fine scale, a neural network was trained to estimate the wavelet coefficients, from which a super-resolution map was reconstructed. Tatem et al. (2002) extended their neural network approach to account for indicator variogram models. Atkinson (2001) and Makido and Shortridge (2005) adopted a swapping algorithm, as used in spatial simulated annealing, to construct plausible super-resolution maps. In these latter works, the coarse fractions were matched exactly by construction. This was achieved by applying the swapping algorithm to an initial purely random super-resolution map comprised of the correct class fractions within each coarse pixel.

The common concern with the above iterative approaches is their rate of convergence and computational burden, associated with the repetitive evaluation of mismatch between simulated and observed coarse fractions, and most importantly between simulated and expected spatial structure. Other more complex sampling methods, such as Markov Chain Monte Carlo methods and simulated annealing are also iterative, and can become computationally prohibitive due to slow convergence; see, for example, Kaipio and Somersalo (2004). In addition, none of the existing approaches for super-resolution mapping accounts for fine resolution data in the form of a sparse set of class labels at informed fine pixels. The recently developed probability perturbation method of Caers and Hoffman (2006), although still iterative, appears to be less computational expensive, and warrants further attention in the context of super-resolution mapping.

In this paper, we propose a novel approach for super-resolution land cover mapping based on the geostatistical methods of indicator Kriging (Journel, 1983) and indicator stochastic simulation (Journel and Alabert, 1989), accounting explicitly for the resolution difference between the available coarse fractions and the sought-after class labels. The proposed approach: (i) is non-iterative and computationally inexpensive, (ii) offers exact, within round-off errors, reproduction of coarse resolution fractions, (iii) ensures exact reproduction of observed class labels at informed fine resolution pixels that might be available, and (iv) closely reproduces a set of indicator variogram models linked to transition probabilities of class labels from one fine pixel to another. Since we explicitly acknowledge that there are multiple solutions to super-resolution land cover mapping, the end product of our method is a set of alternative realizations or maps of class labels having the properties listed above.

Section 2.1 describes the links between the spatial statistics of the fine resolution class labels and the coarse resolution class fractions. These links are exploited in Section 2.2 to derive, via indicator coKriging, the conditional probability of class occurrence at any fine resolution pixel, given the neighboring coarse fractions and possibly some fine resolution sample class labels. In Section 2.3, the coKriging formulation is used within a modified sequential indicator simulation framework to generate alternative realizations of fine resolution class labels with the properties listed above. A case study is provided in Section 3, illustrating the applicability of our proposed methodology for super-resolution land cover mapping using data from a Landsat TM scene over SE China. Last, we offer some discussion and recommendations for future work in Section 4.

2 Methodology

Let $c(v)$ denote the, usually unknown, class at a generic fine resolution pixel $v = v(\mathbf{u})$, with $\mathbf{u}$ being the coordinate vector of its centroid; the area of that pixel v is denoted as $|v|$. It is assumed that at this fine resolution $c(v)$ can take one of K mutually exclusive and collectively exhaustive labels, i.e., $c(v) = k$, with $k = 1, \ldots, K$. The set of all true class labels constitutes the unavailable super-resolution image, and can be arranged in a $(M \times 1)$ vector $\mathbf{c} = [c(v_m), m = 1, \ldots, M]^T$, where superscript T denotes transposition, $M = M_x M_y$ denotes the number of fine resolution pixels, and $v_m = v(\mathbf{u}_m)$. The presence or absence of the k-th class label at pixel v can be coded by a binary class indicator $i_k(v)$, defined as $i_k(v) = 1$, if $c(v) = k$, zero if not. The set of all true indicators for the k-th class can be arranged in a $(M \times 1)$ vector $\mathbf{i}_k = [i_k(v_m), m = 1, \ldots, M]^T$; there are K such vectors (binary images), one per class.

Let $a_k(V)$ denote the fraction of the k-th class at a generic coarse resolution pixel $V = V(\mathbf{s})$, with $\mathbf{s}$ being the coordinate vector of its centroid. The set of all fraction values for the k-th class constitutes the available coarse resolution fraction image, and can be arranged in a $(N \times 1)$ vector $\mathbf{a}_k = [a_k(V_n), n = 1, \ldots, N]^T$, with

$N = N_x N_y$ denoting the number of coarse pixels, and $V_n = V(\mathbf{s}_n)$; there are K such fraction vectors (images), one per class. We denote as $F = |V|/|v| = M/N >> 1$ the resolution ratio between the coarse and fine resolution images, and we assume that both images are co-registered in such a way that there are always F fine resolution pixels $\{v_m, m = 1, \ldots, F\}$ in any coarse resolution pixel V. For simplicity, we do not always use the full notation v_m^n to indicate that the fine pixel v_m belongs to the coarse pixel V_n.

In addition to the coarse resolution fraction images, we consider the case whereby the analyst has access to class labels obtained at a subset of $G << M$ fine resolution pixels. We therefore distinguish between informed and uninformed fine pixels, and denote as $j_k(v_g)$ the sampled k-th class indicator at an informed fine pixel $v_g = v(\mathbf{u}_g)$; again, $j_k(v_g) = 1$, if $c(v_g) = k$, zero if not. The G indicators for the k-th class are arranged into a $(G \times 1)$ vector $\mathbf{j}_k = [j_k(v_g), g = 1, \ldots, G]^T$; there are K such vectors, one per class. It should be stressed that our method does not require availability these latter fine resolution data; if such data are available, our method can readily incorporate them.

In order to condense notation for subsequent discussion, we denote as $\mathbf{d}_k = [\mathbf{a}_k^T \ \mathbf{j}_k^T]^T$ the $((N+G) \times 1)$ vector containing both coarse resolution fraction data and fine resolution sample indicators for the k-th class. There are K such vectors, one per class, which can be arranged in a single $((N+G) \times K)$ matrix $\mathbf{d} = [\mathbf{d}_k, k = 1, \ldots, K]$. With this concise notation, the super-resolution mapping objective can be formulated as the task of finding the $(M \times 1)$ vector $\mathbf{c}$ from the $((N+G) \times K)$ matrix $\mathbf{d}$. Note again, that when the fine resolution sample indicators are not available, matrix $\mathbf{d}$ is of dimension $(N \times K)$ consisting only of class fraction values, but the objective and notation remain the same.

2.1 Statistics of class indicators and fractions

The spatial distribution of the k-th class at the fine resolution is partially characterized by: (i) its proportion, and (ii) a measure of its spatial structure or texture. In this work, we denote as π_k the stationary proportion of the k-th class, and as $2\gamma_k^v(\mathbf{h}) = 2\gamma_k^v(\mathbf{u} - \mathbf{u}')$ the stationary variogram of the k-th class indicators between any two generic (informed or not) fine resolution pixels v and v', whose respective centroids $\mathbf{u}$ and $\mathbf{u}'$ are separated by vector $\mathbf{h} = \mathbf{u} - \mathbf{u}'$; superscript v denotes that the indicator variogram $2\gamma_k^v(\mathbf{h})$ pertains to the fine spatial resolution of v-pixels. The indicator variogram between two particular informed fine pixels v_g and $v_{g'}$ is then denoted as $2\gamma_k^v(\mathbf{u}_g - \mathbf{u}_{g'}) = 2\gamma_k^v(\mathbf{h}_{gg'})$, whereas the indicator variogram between a particular uninformed fine pixel v_m and a particular informed fine pixel v_g is denoted as $2\gamma_k^v(\mathbf{u}_m - \mathbf{u}_g) = 2\gamma_k^v(\mathbf{h}_{mg})$. Similarly, the indicator variogram between two particular uninformed fine pixels v_m and $v_{m'}$ is denoted as $2\gamma_k^v(\mathbf{u}_m - \mathbf{u}_{m'}) = 2\gamma_k^v(\mathbf{h}_{mm'})$.

The indicator variogram $2\gamma_k^v(\mathbf{h})$ characterizes the joint probability of any two

generic fine pixels separated by vector $\mathbf{h}$ to have different class labels. That indicator variogram is readily linked to the probability of transition of class k from any pixel v to a different class k' at any other pixel v', when the two pixel centroids are separated by vector $\mathbf{h}$; see, for example, Carle and Fogg (1996). The joint spatial dissimilarity of two different classes k and k' can be characterized by their indicator cross-variogram $2\gamma^{v}_{kk'}(\mathbf{h})$; although possible, we do not consider such measures of spatial dissimilarity in this work.

We further assume that one has already inferred a parametric model $2\gamma^{v}_{k}(\mathbf{h};\boldsymbol{\theta})$ for the fine resolution variogram of each class k. Here $\boldsymbol{\theta}$ denotes a vector of model parameters, such as sill, range, nugget contribution, and possibly anisotropy direction and ratio. The inference of such a variogram model could be based on fine resolution information, such as aerial photographs acquired in similar scenes and/or possibly ground-based data. Alternatively, one could have information on the functional form of such a variogram model, say, exponential with a nugget component, and then iteratively fit this model to the coarse fractions, along the lines used by Journel and Huijbregts (1978) and Atkinson and Curran (1995). It should be noted here, that we assume that ground-based surveys do not yield an exhaustive sampling of fine resolution land cover over the study area, but only provide partial information on the occurrence of class labels at a sparse set of fine pixels. In most real-world situations, the sampling density of these ground-based surveys might not be sufficient to allow quantifying fine resolution spatial variability. In these cases, one needs to resort to assumptions or expert knowledge to infer the indicator variogram models at that fine resolution; see the discussion in Section 4.

Turning our attention to the coarse resolution data, the fraction value $a_k(V_n)$ for the k-th class at the n-th coarse pixel V_n is formally defined as the average of the k-th class indicators at the F fine pixels within that coarse pixel V_n:

$$a_k(V_n) = \frac{1}{F}\sum_{m=1}^{F} i_k(v_m), \quad v_m \in V_n \tag{1}$$

The spatial distribution of the k-th class fractions is again partially characterized by their mean (expected value) and a measure of their spatial structure. More precisely, the mean $\bar{a}_k$ of the k-th class fraction values equals the corresponding proportion π_k of same class indicators:

$$\bar{a}_k = \frac{1}{N}\sum_{n=1}^{N} a_k(V_n) = \frac{1}{N}\sum_{n=1}^{N}\left[\frac{1}{F}\sum_{m=1}^{F} i_k(v_m)\right] = \frac{1}{M}\sum_{m=1}^{M} i_k(v_m) = \pi_k \tag{2}$$

The fine-to-coarse resolution variogram between the k-th class indicator $i_k(v_m)$ at the m-th fine pixel v_m and the k-th class fraction $a_k(V_n)$ at the n-th coarse pixel V_n

is then computed from the fine resolution indicator variogram model $2\gamma_k^v(\mathbf{h};\boldsymbol{\theta})$ as:

$$2\gamma_k(v_m, V_n) = \frac{1}{F}\sum_{m'=1}^{F} 2\gamma_k^v(\mathbf{h}_{mm'};\boldsymbol{\theta}), \quad v_{m'} \in V_n \tag{3}$$

where the fine pixel v_m need not lie within the coarse pixel V_n.

The above fine-to-coarse resolution variogram is stationary because: (i) the fine resolution variogram $2\gamma_k^v(\mathbf{h};\boldsymbol{\theta})$ is stationary, and (ii) the coarse pixel size defining the integration domain is constant. This entails that the fine-to-coarse resolution variogram is also a function of the separation vector $\mathbf{h}_{mn} = \mathbf{u}_m - \mathbf{s}_n$ between the centroids $\mathbf{u}_m$ and $\mathbf{s}_n$ of pixels v_m and V_n, i.e., $2\gamma_k(v_m, V_n) = 2\gamma_k(v(\mathbf{u}_m), V(\mathbf{s}_n)) = 2\gamma_k^{vV}(\mathbf{u}_m - \mathbf{s}_n) = 2\gamma_k^{vV}(\mathbf{h}_{mn})$; superscript vV indicates that $2\gamma_k^{vV}(\mathbf{h}_{mn})$ is a cross-resolution variogram between fine v-pixels and coarse V-pixels. The cross-resolution variogram between the g-th informed fine pixel v_g and the n-th coarse pixel V_n is computed in the same way as in Equation (3), and is denoted as $2\gamma_k^{vV}(\mathbf{h}_{gn})$.

Last, the variogram between the k-th class fractions at two particular coarse pixels V_n and $V_{n'}$ can be computed from the fine resolution indicator variogram model $2\gamma_k^v(\mathbf{h};\boldsymbol{\theta})$ as:

$$2\gamma_k(V_n, V_{n'}) = \frac{1}{F^2}\sum_{m=1}^{F}\sum_{m'=1}^{F} \gamma_k^v(\mathbf{h}_{mm'};\boldsymbol{\theta}), \quad v_m \in V, \text{ and } v_{m'} \in V' \tag{4}$$

where, again, that coarse resolution variogram is stationary. This entails that the above coarse resolution variogram is also a function of the separation vector $\mathbf{h}_{nn'} = \mathbf{s}_n - \mathbf{s}_{n'}$ between the centroids $\mathbf{s}_n$ and $\mathbf{s}_{n'}$ of pixels V_n and $V_{n'}$, i.e., $2\gamma_k(V_n, V_{n'}) = 2\gamma_k(V(\mathbf{s}_n), V(\mathbf{s}_{n'})) = 2\gamma_k^V(\mathbf{s}_n - \mathbf{s}_{n'}) = 2\gamma_k^V(\mathbf{h}_{nn'})$; superscript V indicates that $2\gamma_k^V(\mathbf{h}_{nn'})$ is a coarse resolution variogram between coarse V-pixels.

Both Equations (3) and (4) are classically derived from the variogram definition and the functional relationship of Equation (1) linking fine resolution indicators with coarse resolution fractions (Journel and Huijbregts, 1978; Atkinson and Curran, 1995). In what follows, the variogram models for the fine resolution class indicators, the fine-to-coarse variograms between such class indicators and the corresponding coarse fractions, and the variograms between the coarse fractions, are used to estimate the probability of class occurrence at any fine resolution pixel.

2.2 Indicator CoKriging

CoKriging with coarse resolution fraction data $a_k(V)$ and, if available, fine resolution class indicator data yields an approximation $\hat{p}_k(v)$ to the true probability $p_k(v) = Prob\{I_k(v) = 1|\mathbf{d}_k\}$ of k-th class occurrence at any fine resolution pixel v (Journel, 1983; Goovaerts, 1997); here $I_k(v)$ denotes a binary random variable at pixel v. That

probability $\hat{p}_k(v)$ is expressed as a weighted linear combination of coarse fractions and fine indicators for the k-th class. Because the class proportions are assumed known, or estimated with sufficient confidence by the mean of the corresponding fraction values, see Equation (2), we consider the simple Indicator CoKriging (ICK) estimate for the m-th fine pixel v_m, written as:

$$\hat{p}_k(v_m) = \boldsymbol{\eta}_k(v_m)^T \mathbf{a}_k + \boldsymbol{\lambda}_k(v_m)^T \mathbf{j}_k + \pi_k \left[1 - \boldsymbol{\eta}_k(v_m)^T \mathbf{1}_N - \boldsymbol{\lambda}_k(v_m)^T \mathbf{1}_G\right] \qquad (5)$$

where $\boldsymbol{\eta}_k(v_m) = [\eta_n^k(v_m), n = 1, \ldots, N]^T$ denotes the $(N \times 1)$ vector of weights assigned to the N fractions for the k-th class, $\boldsymbol{\lambda}_k(v_m) = [\lambda_g^k(v_m), g = 1, \ldots, G]^T$ denotes the $(G \times 1)$ vector of weights assigned to the G informed fine pixels; $\mathbf{1}_N$ and $\mathbf{1}_G$ denote, respectively, a $(N \times 1)$ and a $(G \times 1)$ vector of ones. The known class proportion π_k receives as weight the complement to one of the sum of the weights attributed to the N class fractions and the G class indicators.

The ICK weights $\boldsymbol{\lambda}_k(v_m)$ and $\boldsymbol{\eta}_k(v_m)$ for the k-th class are obtained by solving the following system of equations (ICK system):

$$\begin{bmatrix} \boldsymbol{\Gamma}_k^{VV} & \boldsymbol{\Gamma}_k^{vV} \\ \boldsymbol{\Gamma}_k^{Vv} & \boldsymbol{\Gamma}_k^{vv} \end{bmatrix} \begin{bmatrix} \boldsymbol{\eta}_k(v_m) \\ \boldsymbol{\lambda}_k(v_m) \end{bmatrix} = \begin{bmatrix} \boldsymbol{\gamma}_k^{vV} \\ \boldsymbol{\gamma}_k^{vv} \end{bmatrix} \qquad (6)$$

where $\boldsymbol{\Gamma}_k^{VV} = [2\gamma_k^V(\mathbf{h}_{nn'}), n = 1, \ldots, N, n' = 1, \ldots, N]$ is a $(N \times N)$ matrix of fraction variogram values between all pairs of coarse pixels, $\boldsymbol{\Gamma}_k^{vv} = [2\gamma_k^v(\mathbf{h}_{gg'}), g = 1, \ldots, G, g' = 1, \ldots, G]$ is a $(G \times G)$ matrix of indicator variogram values between all pairs of informed fine pixels, $\boldsymbol{\Gamma}_k^{vV} = [2\gamma_k^{vV}(\mathbf{h}_{gn}), g = 1, \ldots, G, n = 1, \ldots, N]$ is a $(G \times N)$ matrix of variogram values between all pairs of informed fine and coarse pixels, and $\boldsymbol{\Gamma}_k^{Vv} = [\boldsymbol{\Gamma}_k^{vV}]^T$. Term $\boldsymbol{\gamma}_k^{vV} = [2\gamma_k^{vV}(\mathbf{h}_{mn}), n = 1, \ldots, N]^T$ denotes a $(N \times 1)$ vector of variogram values between the m-th uninformed fine pixel v_m and the N coarse pixels, and term $\boldsymbol{\gamma}_k^{vv} = [2\gamma_k^v(\mathbf{h}_{mg}), g = 1, \ldots, G]^T$ denotes $(G \times 1)$ vector of variogram values between the m-th uninformed fine pixel v_m and the G informed fine pixels.

Equations (5) and (6) account for both the coarse resolution class fraction data and (if available) the fine resolution class indicators. Each piece of information, be it a coarse fraction $a_k(V_n)$ or a fine indicator $j_k(v_g)$, is weighted according to its relevance to the unknown same class indicator $i_k(v_m)$ at the uninformed fine pixel v_m. That relevance is quantified by the fine-to-coarse resolution variogram $2\gamma_k^{vV}(\mathbf{h}_{mn})$ for the class fraction $a_k(V_n)$, and by the fine resolution variogram $2\gamma_k^v(\mathbf{h}_{mg})$ for the class indicator $j_k(v_g)$. The ICK weights also account for the redundancy between the data found within the neighborhood of the uninformed fine pixel v_m; that is, for: (i) the correlation between class fractions $a_k(V_n)$ and $a_k(V_{n'})$ at neighboring coarse pixels, (ii) the correlation between class indicators $j_k(v_g)$ and $j_k(v_{g'})$ at neighboring informed fine pixels, and (iii) the correlation between a coarse resolution class fraction $a_k(V_n)$ and a neighboring fine resolution class indicator $j_k(v_g)$.

Since there are K classes, a set of K systems similar to that given in Equation (6) need to be solved, one per class k. The resulting ICK-based probabilities $\{\hat{p}_k(v_m), k =$

$1, \ldots, K\}$ derived from Equation (5) need to be corrected to ensure that they lie in the $[0, 1]$ interval and have a unit sum; typically, the magnitude of such corrections is very small (Goovaerts, 1997). In addition, these K systems need to be solved M times, one for each fine pixel v_m. Because the number N of class fraction data is typically large, the above systems are solved using a limited amount of such data, most often those falling in a neighborhood centered on the coarse pixel V_n containing the fine pixel v_m where ICK is performed. The extent of that neighborhood is typically linked to the range of the class fraction variograms (Goovaerts, 1997).

Since Kriging is an exact interpolator, the ICK-derived probability $\hat{p}_k(v_g)$ at an informed fine pixel v_g yields the corresponding class indicator $j_k(v_g)$, no matter the indicator variogram models $2\gamma_k^v(\mathbf{h}; \boldsymbol{\theta})$ used to compute all the variogram values called for by the ICK system of Equation (6). Equally important for consistency, the average of the ICK-derived probabilities of class occurrence within any given coarse pixel V_n reproduces the corresponding class fraction:

$$\frac{1}{F} \sum_{m=1}^{F} \hat{p}_k(v_m) = a_k(V_n), \quad v_m \in V_n \tag{7}$$

see Mao and Journel (1998) for a proof, as well as Kyriakidis and Yoo (2005) for a generalization of that proof. The above reproduction holds only if the ICK-derived probabilities are not corrected to lie in the $[0, 1]$ interval and sum to one. If such a correction is performed, then Equation (7) becomes approximate, yet in practice very close to being true; see Mao and Journel (1998), as well as the case study of this paper.

If no fine resolution class indicators are available ($G = 0$), the ICK estimate $\hat{p}_k(v_m)$ of Equation (5) simplifies to:

$$\hat{p}_k(v_m) = \boldsymbol{\eta}_k(v_m)^T \mathbf{a}_k + \pi_k \left[1 - \boldsymbol{\eta}_k(v_m)^T \mathbf{1}_N\right] \tag{8}$$

where it should be stressed that the resulting prediction is not the same as that given in Equation (5) because the data used are not the same in these two cases; here we use the same notation for simplicity.

The corresponding ICK weights are simply found by reducing Equation (6) to:

$$\boldsymbol{\Gamma}_k^{VV} \boldsymbol{\eta}_k(v_m) = \boldsymbol{\gamma}_k^{vV} \tag{9}$$

and the reproduction of the coarse resolution class fraction by the resulting ICK probabilities is still guaranteed, i.e., Equation (7) still applies, no matter the fine resolution indicator variogram models $2\gamma_k^v(\mathbf{h}; \boldsymbol{\theta})$ used to compute the entries of matrix $\boldsymbol{\Gamma}_k^{VV}$ and vector $\boldsymbol{\gamma}_k^{vV}$ in Equation (9).

The Kriging component of the approach developed by Verhoeye et al. (2001) can now be viewed within the proposed geostatistical framework. More precisely, in

that work the authors estimated $\hat{p}_k(v_m)$, which they termed a spatial dependence parameter, by replacing the right hand side vector $\boldsymbol{\gamma}_k^{vV}$ in the system of Equation (9) by $\boldsymbol{\gamma}_k^{VV}$; this modification amounts to ignoring the resolution difference between the original coarse fractions and the target super-resolution map. As a consequence, any integration of coarse resolution fractions with fine resolution indicators would not be straightforward, as opposed to our method which readily allows for such a fusion.

On the computational side, if no fine resolution indicators are available, the weights vector $\boldsymbol{\eta}_k(v_m)$ can be found by solving much fewer ICK systems than the number M of fine resolution pixels (Kyriakidis and Yoo, 2005). This is a consequence of the fact that, for a given indicator variogram model $2\gamma_k^v(\mathbf{h};\boldsymbol{\theta})$, the ICK weights are only function of the spatial data configuration (the pixel layout), not of the actual data values. Since all fine pixels within a coarse pixel have the same coarse neighbors (ignoring edge effects) as any other set of fine pixels within another coarse pixel, that data configuration remains the same.

We do not recommend turning the Kriging-derived probabilities into a set of class labels by some form of, say, Maximum a Posteriori (MAP) allocation rule. Indeed, super-resolution land cover mapping is much more than per-pixel classification, in that it deals with *joint* classification under coarse fraction reproduction constraints; that is, with the task of creating land cover maps consistent with all available information.

2.3 Sequential indicator simulation

One efficient simulation algorithm for generating synthetic categorical maps, given a sample set of known categories and a set of indicator variogram models, is sequential indicator simulation (Journel and Alabert, 1989; Goovaerts, 1997), abbreviated here as SIS. The key paradigm in SIS is the decomposition of the multivariate probability distribution $f(\mathbf{i}_k|\mathbf{d}_k)$ of M indicator RVs $\{I_k(v_m), m = 1,\ldots,M\}$ into a product or sequence of M univariate conditional probabilities as:

$$\begin{aligned} f(\mathbf{i}_k|\mathbf{d}_k) &= Prob\left\{I_k(v_1) = i_k(v_1),\ldots,I_k(v_M) = i_k(v_M)|\mathbf{d}_k\right\},\ k = 1,\ldots,K \quad (10) \\ &= \prod_{m=1}^{M} Prob\left\{I_k(v_m) = 1|\mathbf{i}_k^{m-1},\mathbf{d}_k\right\},\quad k = 1,\ldots,K \end{aligned}$$

where $Prob\left\{I_k(v_m) = 1|\mathbf{i}_k^{m-1},\mathbf{d}_k\right\}$ is the univariate conditional probability of the m-th indicator RV $I_k(v_m)$, given: (i) the $m-1$ previously simulated indicator values stored in a $((m-1)\times 1)$ vector $\mathbf{i}_k^{m-1} = [i_k(v_{m'}), m' = 1,\ldots,m-1]^T$, and (ii) the original data vector $\mathbf{d}_k$ comprised of the N coarse resolution fractions and possibly the G fine resolution sample indicators for the k-th class. In this paper, any such univariate conditional distribution is determined by ICK; see Section 2.2.

Simulation proceeds along a, typically random, path which considers in sequence the M fine resolution pixels, and thus determines the order of the decomposition given

in Equation (10). At any fine pixel, say v_m, along that path, a simulated class label $c^{(l)}(v_m)$ is generated from the corresponding K ICK-derived conditional probabilities at that pixel; here superscript (l) denotes the l-th simulated value, and there can be L such values. The associated K simulated indicators $\{i_k^{(l)}(v_m), k = 1, \ldots, K\}$ are then considered as data which constrain all subsequent univariate conditional probabilities, and hence all subsequent simulated class labels generated from such probabilities.

The end product of repeating the above steps at all M fine resolution pixels is a simulated realization of class labels denoted as $\mathbf{c}^{(l)} = [c^{(l)}(v_m), m = 1, \ldots, M]^T$. A new class realization $\mathbf{c}^{(l')}$ can be generated by repeating the above procedure with a different random path. Because any simulated class label conditions or constrains the generation of all subsequent labels along the simulation path, spatial continuity is ensured. More precisely, the simulated class maps $\{\mathbf{c}^{(l)}, l = 1, \ldots, L\}$ reproduce in expected value the K fine resolution indicator variogram models $\{2\gamma_k^v(\mathbf{h}; \boldsymbol{\theta}), k = 1, \ldots, K\}$; for more details, the reader is referred to Goovaerts (1997).

Although the ICK-derived probabilities are consistent with the coarse resolution fractions, see Equation (7), this characteristic does not translate to the simulated classes themselves, because the latter are derived via a non-linear operation (thresholding) from the ICK-derived probabilities. This entails that a simulated super-resolution class map $\mathbf{c}^{(l)}$ may not reproduce when upscaled the corresponding class fractions at the coarse resolution. That reproduction is achieved in expected value; that is, on average over many realizations. A correction is therefore needed to ensure that the proportion of simulated fine resolution class indicators within the coarse pixels reproduce the corresponding fraction data. In what follows, we propose a progressive correction algorithm to enforce that reproduction exactly.

More precisely, consider the m-th fine pixel v_m^n visited along the simulation path; superscript n indicates that this pixel lies within the coarse pixel V_n. Let $p_k^R(v_m^n)$ denote the current (prior to visiting the m-th pixel v_m) remaining proportion of fine pixels within V_n that, given the coarse fraction $a_k(V_n)$, should be simulated as belonging to the k-th class:

$$p_k^R(v_m^n) = \frac{int[a_k(V_n)F] - \sum_{m=1}^{F_{m-1}(V_n)} i_k(v_m^n)}{F - F_{m-1}(V_n)}, \quad \in [0,\ a_k(V_n)] \tag{11}$$

where $int[\cdot]$ denotes rounding to the nearest integer, $F_{m-1}(V_n)$ denotes the number of fine pixels within V_n that have already been visited prior to arriving at the m-th pixel v_m^n. The running proportion $p_k^R(v_m^n)$ can also be regarded as the probability of simulating a fine pixel as belonging to the k-th class, given: (i) the number of fine pixels within V_n already simulated as belonging to that class, and (ii) the target coarse fraction value $a_k(V_n)$. This running proportion can thus be viewed as a saturation probability for a particular coarse pixel v_m in the k-th class, and depends on how

many fine pixels have already been simulated as belonging to class k within that coarse pixel.

Our correction algorithm combines the ICK-derived conditional probability of Equation (5), denoted here as $p_k^{IK}(v_m^n)$, with the running proportion $p_k^R(v_m^n)$ of Equation (11) using a multiplicative rule for probability fusion (Bordley, 1982; Benediktsson and Swain, 1992; Journel, 2002):

$$Prob\{I_k(v_m^n) = 1 | \mathbf{i}_k^{m-1}, \mathbf{d}_k\} = \frac{p_k^{IK}(v_m^n) p_k^R(v_m^n)}{a_k(V_n) \;\; S}$$
$$\text{where} \;\; S = \frac{\sum_{k=1}^{K} p_k^{IK}(v_m^n) p_k^R(v_m^n)}{a_k(V_n)} \tag{12}$$

When no fine pixels within V_n have been simulated as belonging to class k, $p_k^R(v_m^n) = a_k(V_n)$, hence Equation (12) leaves the ICK-derived probability $p_k^{IK}(v_m^n)$ unchanged. As simulation progresses along the random path, the correction of Equation (12) may become more important if $p_k^R(v_m^n)$ differs significantly from the target proportion $a_k(V_n)$. When the proportion of fine pixels within V_n simulated as belonging to class k reaches the target fraction $a_k(V_n)$, then $p_k^R(v_m^n) = 0$, and the combined probability of Equation (12) is also zero. This algorithm therefore constrains the proportion of simulated fine resolution class labels within V_n to reproduce exactly the corresponding coarse fraction $a_k(V_n)$.

It should be stressed that our proposed method is fast when compared to other iterative methods for super-resolution mapping. This speed advantage is due to: (i) the SIS algorithm being a single-pass simulation method: there is no iteration involved in generating plausible alternative class realizations, and (ii) the algorithm used to enforce the reproduction of coarse resolution fractions also being non-iterative.

3 Case study

To demonstrate our proposed super-resolution mapping approach, we consider a reference land cover classification derived from a Landsat TM scene of an area in the Pearl River Delta, South East China; see Seto et al. (2002) for more details. The reference land cover class map, shown in Figure 1, has dimension 15km×15km, and includes 500×500 fine resolution pixels. Each pixel has size $30m \times 30m$, and is considered as belonging to one of $K = 3$ broadly defined land cover classes: vegetation (white color, with regional proportion 0.52), urban (grey color, with proportion 0.18), bare soil (black color, with proportion 0.30).

It should be noted that the reference map considered in this case study was chosen for illustrative purposes. In other real-world applications, the true land cover classification could be far more complex and contain more classes, e.g., here, water. Our approach can handle an arbitrary number of classes, and arbitrarily complex

indicator variogram models; of course, for a given resolution ratio F, the associated computational burden increases as a function of the number of classes and variogram model complexity (Goovaerts, 1997). As stated above, the intent of this case study is to demonstrate the construction of multiple super-resolution maps from the available coarse and fine resolution information, not to make the most locally accurate super-resolution land cover map for the particular region.

The reference land cover map of Figure 1 was upscaled into three coarse fraction maps using three different fine-to-coarse resolution ratios. For each coarse pixel, the corresponding class fractions are computed as the linear average of the fine pixel class indicators within that coarse pixel. More precisely, each coarse pixel is progressively comprised of $9 \times 9 = 81$, $15 \times 15 = 225$ and $25 \times 25 = 625$ fine pixels, with associated pixel size 270m $\times$ 270m, 450m $\times$ 450m and 750m $\times$ 750m; the resulting sets of coarse class fraction maps are shown in Figure 2. Since no observational errors are considered in this work, such synthetic fraction maps could be thought of as the outputs of a perfect spectral unmixing of data originating from sensors with coarser spatial resolution than that of Landsat TM.

The reference fine resolution indicator variograms for the three classes (not shown) were inferred from the land cover map of Figure 1. Each indicator variogram was modeled with a nugget effect contribution and two isotropic exponential functions or nested structures. The variogram model parameters, with partial sills given as proportions to a unit sum, are given in Table 1. The nugget effect contributions range from 0.10 to 0.14, indicating that the reference land cover map exhibits a small component of purely random spatial variability. The first exponential structure has ranges from 7 to 12 fine (TM) pixels, and shows similar partial sills across all classes (0.50 to 0.52). The second exponential structure has ranges from 65 to 70 fine pixels, and similar partial sills (0.36 to 0.39). The above variogram model parameters imply that: (i) more than 50% of the class spatial variability at the fine resolution occurs at scales smaller than the coarse pixel size, and (ii) for each upscaling scheme, all spatial variability occurs at scales smaller than eight, five and three coarse pixels, respectively, since $70/9 = 7.78$, $70/15 = 4.67$ and $70/25 = 2.80$.

In general, the larger the upscaling ratio, the less information is carried by the corresponding coarse resolution fractions. Such a loss of information due to averaging is a function of the variogram shape near the origin and its range: the larger that range or the smoother the underlying field, the smaller that information loss (Journel and Huijbregts, 1978). Since more than 50% of spatial variability in the reference land cover map of Figure 1 occurs within 7 to 12 TM pixels, one should expect that the latter two upscaling schemes (15×15 and 25×25) would yield coarse resolution fractions with more or less similar information content. A very significant portion of the spatial information content in the reference land cover map is lost going from the TM pixel size to the first coarse pixel size (9×9 upscaling).

3.1 Kriging

Using the coarse fraction maps of Figure 2, and the fine resolution indicator variogram models whose parameters are given in Table 1, the probabilities for class occurrence at any fine resolution pixel v_m^n that falls within any coarse pixel V_n are computed via ICK; see Equations (8) and (9). The data used for ICK at any such fine pixel v_m^n consist of a set of 21 coarse pixel neighbors defined as the 5×5 coarse template centered at V_n excluding the four corner pixels. That neighborhood geometry was chosen for computational efficiency reasons: the weights received by those four corner pixels are negligible with respect to those received by the remaining pixels in that neighborhood. For each upscaling scheme, the resulting set of three probability maps, one for each class, is shown in Figure 3. As expected from theory, these Kriging-derived probability maps reflect the conditioning fraction data of Figure 2 without any block artifacts. The smooth transition between the ICK-derived probabilities computed at fine pixels within two adjacent coarse pixels V and V' is a consequence of considering the closest 21 neighboring coarse fraction data. If only the co-located coarse fractions $a_k(V)$ and $a_k(V')$ had been considered, strong discontinuities would be visible in the probability maps of Figure 3 near the coarse pixel boundaries.

The high frequency spatial variability seen on the reference land cover map of Figure 1, however, is not reproduced by the ICK-derived probability maps of Figure 3, especially for the larger upscaling ratio. This is as expected due to the smoothing effect of Kriging and any interpolation algorithm in general. If one was to perform class allocation (using, say, a MAP criterion) by thresholding the ICK-derived probabilities of Figure 3, the spatial distribution of the resulting classes would have a much smoother spatial distribution than that seen in the reference land cover map of Figure 1. For a more detailed discussion of spatial prediction (Kriging) versus simulation, the reader is referred to Goovaerts (1997).

To check the consistency of the Kriging-based downscaling procedure in reproducing the coarse class fractions, the ICK-derived probabilities for the 25×25 upscaling scheme shown in Figure 3(g)-(i) were averaged within each coarse pixel, and compared to the corresponding coarse fractions of Figure 2(g)-(i). Figure 4 shows the resulting scatterplots: as expected from theory, see Equation (7), the coarse fraction data are reproduced; any mismatch is due to round-off errors.

In addition to the coarse fraction data of Figure 2(g)-(i) corresponding to the 25×25 upscaling scheme, five hundred (500) fine resolution sample class labels (not shown) were collected at random from the reference land cover map of Figure 1, and added to the conditioning information. ICK, see Equations (5) and (6), was now performed using the same 21 coarse pixel neighborhood as above, and all the sample class labels inside a radius of 70 fine resolution pixels or 3 coarse pixels for the 25×25 upscaling scheme. The resulting ICK-derived probabilities are shown in Figure 5. The introduction of the 500 fine resolution class labels did not affect the results significantly, except in the immediate vicinity of these fine resolution data;

compare Figures 3(g)-(i) and 5(a)-(c). Had the fine resolution indicator variogram models exhibited smaller nugget contributions and longer ranges, or had the 500 fine resolution class labels been preferentially located as clusters close to distinct features of the reference class map of Figure 1, the local differences between Figures 3 and 5 would have been larger. When the fine resolution ICK-derived probabilities of Figure 5 are averaged within each corresponding coarse pixel, they reproduce the coarse fractions seen in the last row of Figure 2; that reproduction yields a set of scatterplots (not given here) similar to those shown in Figure 4.

3.2 Sequential simulation

Next, sequential indicator simulation (SIS) with the progressive correction algorithm of Equation (12) was performed, see Section 2.3, yielding multiple super-resolution realizations of land cover. The data used to generate these realizations were: (i) the different sets of coarse fraction images displayed in Figure 2, and (ii) the fine resolution indicator variogram models whose parameters are given in Table 1.

Three sets of such super-resolution realizations are shown in Figure 6; the realizations in each row were generated using the corresponding row of coarse fraction images shown in Figure 2 as conditioning data. Despite the significant differences in input information provided by the coarse fraction images, the resulting super-resolution maps of Figure 6 exhibit similar spatial patterns. One can accept, at least visually, that these simulated maps reproduce the low frequency spatial patterns of the reference land cover map of Figure 1. Bare soil (black color), for example, occurs in patches attached to the more elongated urban class (grey color). In addition, the high frequency spatial patterns (texture) found in the reference map of Figure 1 are reproduced well in all super-resolution realizations of Figure 6, no matter the coarse fraction images used (i.e., across all upscaling ratios considered); this is not the case with the ICK-derived probability maps shown in Figure 3. As stated above, simulation aims at reproducing the prior model of spatial structure within the constraints of the available data. Since that fine resolution structural model is independent of the resolution of the coarse fractions, and these coarse fractions are consistent with the prior structural model (i.e., the reference indicator variograms were used for simulation), the resulting super-resolution realizations show realistic texture reproduction. Last, because the progressive correction algorithm was employed in generating the super-resolution realizations of Figure 6, the corresponding coarse fractions are reproduced (up to round-off errors) when these fine resolution realizations are upscaled; see Figure 7.

The reproduction of the prior structural model at the target fine resolution is quantitatively investigated in Figure 8, by comparing the indicator variograms of 25 SIS realizations with the input fine resolution indicator variogram models whose parameters are given in Table 1. These 25 realizations were conditioned to the coarse

fraction data of Figure 2(g)-(i) corresponding to the 25×25 upscaling scheme. The indicator variograms shown in Figure 8 are not standardized to a unit sill, to better appreciate the different variance of land cover classes, which is approximately equal to $\pi_k(1 - \pi_k)$ for a given class k. Overall, the indicator variograms computed from the simulated super-resolution maps reproduce the input model variograms; see Figure 8. These super-resolution realizations, however, exhibit a slightly higher degree of short-scale spatial variability; see the nugget contribution mismatch in Figure 8, particularly for the vegetation class. We believe that this mismatch is a consequence of the correction algorithm used to enforce the reproduction of the coarse class fractions of Figure 2(g)-(i), and we are currently investigating alternative procedures for eliminating such a mismatch.

Note that some complex sub-pixel features, e.g., curvilinear roads, found in the reference land cover map of Figure 1 are not seen in the simulated maps of Figure 6. These features are lost during the upscaling procedure, and they cannot be retrieved from the coarse fractions alone without any additional fine resolution information. Such information is beyond that provided by the fine resolution indicator variograms, which can only characterize repetitive spatial patterns with elliptical or circular geometry. For a thorough discussion on the inadequacy of variograms to capture spatial patterns with complex geometrical characteristics, the reader is referred to Strebelle (2002).

The procedure conducted above for checking the reproduction of coarse resolution information, was also repeated for the case of SIS without the incorporation of the progressive correction algorithm. Three such super-resolution realizations, generated using the coarse fraction data of Figure 2(g)-(i) corresponding to the 25×25 upscaling scheme, are shown in Figure 9. Because thresholding of probabilities of class occurrence into actual labels is a non-linear transformation, these realizations do not reproduce the corresponding coarse fractions when upscaled; see Figure 10(a)-(c). However, globally and for all classes, the upscaled simulated coarse fractions are unbiased; that is, the differences between simulated and observed coarse class fractions have a near zero mean. In addition, the super-resolution maps of Figure 9 reproduce the input indicator variogram models better than the realizations shown in Figure 6(g)-(i); compare Figure 10(d)-(f) to Figure 8(g)-(i). Note also that the indicator variograms of the simulated super-resolution maps fluctuate more when the correction algorithm is not used, because these simulated realizations are not as tightly constrained by the coarse fractions.

The same 500 fine resolution class labels used to derive the ICK probabilities of Figure 5 were also considered, along with the coarse fractions of Figure 2(g)-(i), for generating another set of realizations via SIS and the progressive correction algorithm of Equation (12); three such realizations are shown in Figure 11. Due to the application of the correction algorithm, the coarse fractions of Figure 2(g)-(i) are reproduced when the super-resolution realizations of Figure 11 are upscaled; the

corresponding scatterplots are very similar to those given in Figure 7, and are not given here. The simulated super-resolution maps of Figure 11 should be compared to the reference map of Figure 1 and the simulated maps shown in the bottom row of Figure 6. There are some visible local differences between the three corresponding realizations of Figure 6(g)-(i) and Figure 11, but no systematic difference can be detected overall.

To illustrate the impact of different prior models of spatial structure on the resulting super-resolution maps, we consider two new sets of fine resolution indicator variogram models; recall that the parameters of the reference indicator variogram models were given in Table 1. The first set of new variograms consists of pure nugget effect models, whereas the second set consists of exponential models with no nugget contribution and ranges equal to 500 fine pixels; that is, approximately 7 times larger than the largest range of the reference models. The former models correspond to an assumption of purely random spatial variation of classes, whereas the latter models correspond to an assumption of strong continuity of such classes.

To better appreciate the spatial structure associated with these different sets of indicator variogram models in the absence of conditioning data, three unconditional realizations are given in Figure 12(a)-(c); these were generated without accounting for any coarse fraction data or class labels at some informed fine resolution pixels, hence the term unconditional. Figure 12(a) exhibits the characteristic "salt and pepper" texture of a white noise image, whereas Figure 12(c) exhibits class labels that are spatially arranged in very large patches. The same sets of indicator variogram models were subsequently used to generate the three conditional realizations shown in Figure 12(d)-(f). Because these realizations were conditioned to the coarse fraction data shown in Figure 2(g)-(i) corresponding to the 25×25 upscaling scheme, they reproduce these coarse fraction values when upscaled. The differences between Figures 12(a)-(c) and 12(d)-(f) lie in the effect of the conditioning coarse fraction data. It is precisely the information carried by these coarse fractions that forces the spatial patterns of land cover classes to be located where they do in the latter set of realizations. Note that the simulated super-resolution map of Figure 12(f) exhibits significantly different spatial patterns than those implied by the prior model of spatial structure, and depicted in Figure 12(c). Indeed, in our proposed super-resolution mapping method, the data (i.e., the coarse fraction values in this case) exert a far greater influence on the spatial patterns of the resulting super-resolution maps than the prior model of spatial structure adopted. In the case of Figure 12(f), that prior model of spatial structure was inconsistent with the observed coarse fractions, since these fractions were generated from the reference land cover map of Figure 1 whose indicator variograms did not imply a very strong spatial continuity. Consequently, one can conclude that the coarse fraction data (not the prior model) dominate the patterns found in the super-resolution land cover map of Figure 12(f).

Comparing the various conditional realizations, one can easily appreciate that Fig-

ure 12(d), which corresponds to the assumption of lack of spatial correlation, differs clearly (exhibits more fragmented classes) from Figures 12(e)-(f) which correspond to prior models of spatial structure with significant spatial auto-correlation. Figures 12(e) and (f) differ slightly in the extent of class patches, the latter exhibiting somewhat larger patches (less fragmentation) than the former due to the assumption of stronger spatial continuity.

To corroborate the above statements, the reference land cover map of Figure 1 was first converted into three binary images of class indicators. Each binary image was then subjected to connected components labeling (using 8-point connectivity) to define objects comprised of groups of *connected* pixels with the same class indicator; see, for example, Gonzalez and Woods (2002). The natural logarithm of the areas of objects found in each binary image was finally recorded for the corresponding land cover class. The histogram of such object areas can be viewed as a measure of spatial structure going beyond that encapsulated in the indicator variogram models. The same connected components labeling procedure was then applied to the simulated super-resolution maps of Figure 12(d)-(f). The distributions of the natural logarithm of object areas derived from the reference and from the three simulated land cover maps were then compared using the quantile-quantile (Q-Q) plots given in Figure 13. Quantiles for object areas derived from the reference land cover map pertain to the x-axes of these plots, whereas quantiles derived from object areas found in the simulated maps pertain to the y-axes of these plots. A perfect agreement between the distributions of reference and simulated object areas would entail a Q-Q plot with bullets aligned on the diagonal solid line or first bisector. When a simulated super-resolution map exhibits more (less) fragmentation than the reference land cover map, the bullets of the associated Q-Q plot are aligned below (above) the diagonal line.

Figure 13(a)-(c) corroborates that the simulated super-resolution map of Figure 12(d) exhibits much more class fragmentation than the reference land cover map of Figure 1: the Q-Q plots for all classes are well below the diagonal lines, indicating simulated objects with smaller areas than those found in the reference map. Figures 13(d)-(f) and 13(g)-(i) show a much better agreement between simulated and reference object areas than that found in Figure 13(a)-(c), indicating that a purely random model of spatial structure is inappropriate as expected. Comparing Figures 13(d)-(f) and 13(g)-(i), one can generally conclude that the two super-resolution maps of Figure 12(e) and (f) do not have significantly different spatial patterns, since the corresponding Q-Q plots are more or less aligned with the diagonal lines. Only some small differences can be detected in favor of the super-resolution map of Figure 12(e), in particular for the urban and bare soil classes; compare Figure 13(e)-(f) with Figure 13(g)-(i). In the former plots, the bullets are closer to the diagonal lines, indicating that the prior model of spatial structure based on the reference indicator variograms is slightly better than that based on maximum continuity. Note that this latter statement should be viewed in light of the data control on the simulated realizations:

even if an inappropriate model of spatial structure was adopted, such as that of maximum continuity, the available coarse fractions did not allow the generation of simulated super-resolution maps with large patches of class labels; compare Figure 12(c) with Figure 12(f). As stated above, simulation aims at reproducing a prior model of spatial structure within the constraints of the available data. In this case, the constraints of the coarse fraction data largely over-wrote the inappropriate assumption of maximum continuity.

4 Discussion and conclusions

In this paper, super-resolution land cover mapping is viewed as an under-determined inverse problem, that of constructing fine resolution land cover maps from coarse class fraction data. We document the necessity of a prior model of spatial structure for land cover at the fine (target) resolution to resolve the inherent ambiguity of such an ill-posed inverse problem and make it solvable. In addition, we state that existing super-resolution land cover mapping solutions invoke such a prior model, either explicitly or implicitly. In our work, that prior structural information is explicitly parameterized in terms of a set of indicator variogram models that characterize the spatial variability of land cover classes at the fine resolution. Such variogram models can range from pure nugget effect models, indicative of completely random spatial variation of class labels, to models with extremely large range and no nugget contribution, indicative of strong continuity in the spatial patterns of class labels.

We acknowledge that, even within a given prior model of spatial structure, multiple plausible solutions exist to the super-resolution mapping inverse problem. Consequently, we propose formulating explicitly super-resolution mapping as the task of generating or "exploring" such equally plausible solutions. In addition, we argue that any map of fine resolution class labels that: (i) reproduces the particular set of fine resolution indicator variogram models adopted, (ii) reproduces a typically sparse set of class labels at some informed fine pixels, if available, and (iii) when upscaled, reproduces the corresponding coarse fraction data, constitutes a plausible solution to that inverse problem. To this respect, we developed a novel, non-iterative, geostatistical simulation algorithm for generating such plausible, super-resolution land cover maps.

To some, generating several, instead of a single, super-resolution land cover maps may appear as a drawback. In this work, however, we advocate that one should not be looking for a single best super-resolution map. First and foremost, one needs to decide on what are the constituents of a best map. Almost always, best is cast in terms of per-pixel accuracy with respect to the true land cover map or to some validation samples obtained from it. Alternatively, one might be concerned with the reproduction of spatial patterns of land cover, such as fragmentation or compactness (textural) characteristics of mapped classes. In addition and most importantly, a single super-resolution map does not reveal the uncertainty associated with its con-

struction. The bulk of that uncertainty stems from the lack of abundant data at the target fine spatial resolution, and the difficulty to infer a model of spatial structure at that target resolution. Super-resolution land cover mapping is almost never the end-goal per se; instead, super-resolution maps are intended to serve as inputs to detailed spatial analysis operations, other coupled environmental models, or decision support systems, all requiring input data at that fine resolution. It therefore behoves us to explore the consequences of the uncertainty associated with super-resolution mapping on the outcomes of the above operations or model outputs within an uncertainty propagation or uncertainty analysis context. Our proposed simulation method allows, for example, to explore the uncertainty in the outputs of a fire-spread simulator, due to unavailable or sparse land cover data at the appropriate resolution: this could be achieved by running the fire-spread simulator using multiple super-resolution realizations of land cover, and studying, say, the spatial distribution of the resulting simulated fire fronts.

It should be also stressed that, for a given prior structural model, none of these plausible solution maps is expected to be more accurate than any other, when compared pixel-per-pixel with some validation class labels. As long as the generated super-resolution maps reproduce the available data, they are all equally likely to yield similar accuracy scores in a validation test. Of course this statement involves expectation: a particular solution map might yield a higher accuracy score than some other, but on average it is expected that all solutions generated from the same prior structural information, and accounting for the same data via the same algorithm, have similar degrees of per-pixel mismatch with the true land cover map. From this viewpoint, the concept of accuracy in super-resolution mapping is translated to that of accurate reproduction of coarse and possibly fine data, and of the prior structural model. Of course, there is always the issue of choosing a prior model of spatial structure that accurately encapsulates the expected spatial patterns at the fine resolution within the constrains of the coarse fraction data.

In this paper, the application of our proposed super-resolution mapping method was illustrated via a case study using data from a Landsat TM scene from SE China. Our method, however, can be efficiently used for land cover mapping at any spatial resolution, the only requirements being that: (i) the classes are mutually exclusive and collectively exhaustive, (ii) the classification scheme is valid at both coarse and fine resolutions, and (iii) one has available a prior model of spatial structure for the fine (target) resolution. Requirement (i) entails that there are no fuzzy but only crisply-defined classes, and that these classes cover all possible states that are expected to be found at the fine spatial resolution. For fuzzy classification schemes, one needs to revert to approaches based on fuzzy set theory, although soft labels (e.g., defined by probability intervals) can also be accounted for by soft indicator Kriging (Goovaerts, 1997). When the classes are not deemed collectively exhaustive, one could artificially define an additional class which encompasses labels not classified

in any other class. Requirement (ii) implies that the adopted classes are meaningful, and satisfy requirement (i), at both coarse and fine resolutions. Requirement (iii) may be the most difficult piece of information to obtain in practice, and some guidelines for obtaining it are given hereafter.

The prior model of spatial structure could be directly inferred from a ground survey, if enough informed fine pixels are located at distances smaller than the coarse pixel extent to compute reliable variogram values for sub-pixel lag distances. If such fine resolution sample data are not available, then the prior structural model might be synthesized from analogs, e.g. high resolution imagery obtained from a different sensor in a nearby region with similar land cover classes, or in the same region but in the past. Alternatively, that prior structural information might be built by combining the spatial information from the coarse resolution fractions with some expert opinion on the fine resolution spatial structure. For example, one might deem some classes less continuous or with more high frequency variation than others, such as the urban class in the case study of this paper. Such a type of information could be readily integrated in the fine resolution indicator variogram models by adjusting their relative nugget contributions and/or ranges. Last, one could imagine using land cover predictions from urban simulation models as a possible source of fine resolution textural information.

No matter the source used to acquire this high resolution information of spatial structure, this paper illustrated that any super-resolution mapping attempt is based, either explicitly or implicitly, on the availability of such a model. Consider, for example, the case of simple contouring of coarse fractions to derive a map of fine resolution fractions, or better stated a map of probabilities of class occurrence. This latter procedure fails to acknowledge resolution differences, by incorrectly assuming that the coarse fractions pertain to pixel centroids; this entails that the resulting fine resolution fractions are not guaranteed to reproduce, when upscaled, the corresponding coarse fractions. In addition, that fine resolution fraction map needs to be converted to a map of class labels. Any per-pixel thresholding of such fine resolution fractions into class labels will result in a particular (albeit not defined explicitly) spatial pattern of land cover. In other words, the simple procedure outlined above also invokes implicitly a hidden model of fine resolution spatial structure; that model is embedded in the weights used for contouring the coarse fractions, and in the constraints of contiguity (if any) adopted for the final class allocation step.

We believe it is far better opening the question of how to build a model of fine resolution spatial structure, rather than hiding it under an assumption, such as that of maximum spatial continuity, which is not often questioned because of its convenience. In addition, we strongly suggest that users consider different candidate fine resolution variogram models, possibly constructed from data-based information and/or individual judgement, within a sensitivity analysis or scenario building context. Our proposed approach allows the exploration of such alternative scenarios via

the generation of associated super-resolution land cover maps that can be used in an uncertainty propagation framework as inputs to other coupled environmental models or decision-making procedures.

The methodology presented in this paper would undoubtedly benefit from further research to: (i) fine tune the progressive correction algorithm so that the super-resolution maps reproduce better the indicator variogram models at short distance lags, (ii) account for errors or uncertainty in the coarse fraction maps, (iii) account for a known point spread function of a sensor, and (iv) incorporate other sources of fine resolution information that might be available in the form of contextual information, ancillary data, or analog images.

The algorithms used, namely indicator coKriging and sequential indicator simulation with coarse resolution fractions, were coded as plug-ins into the public domain SGEMS software (Remy, 2004). These plug-ins, the data sets, as well as the parameters files used in this case study can be freely downloaded from the following URL: `http://pangea.stanford.edu/~aboucher/superRes`.

Acknowledgments

The first author acknowledges partial funding from a PhD scholarship from the program: *Fonds Québécois de la recherche sur la nature et les technologies* from the government of Quebec, Canada. The second author acknowledges partial funding provided by the National Science Foundation under Award BCS #0422599. Both authors would like to thank Prof. André Journel at Stanford University for his constructive comments on early versions of this paper. The constructive comments of three anonymous reviewers that helped us improve the originally submitted manuscript are also gratefully acknowledged.

References

Atkinson, P. M., 2001. Super-resolution target mapping from soft-classified remotely sensed imagery. In: *Proceedings of the 6th International Conference on Geocomputation*, University of Queensland, Brisbane, Australia, September 24-26, 2001.

Atkinson, P. M., Curran, P. J., 1995. Defining an optimal size of support for remote-sensing investigations. *IEEE Transactions on Geoscience and Remote Sensing*, 33 (3), 768 – 776.

Atkinson, P. M., Cutler, M. E. J., Lewis, H., 1997. Mapping sub-pixel proportional land cover with AVHRR imagery. *International Journal of Remote Sensing*, 18 (4), 917 – 35.

Bachmann, A., Allgöwer, B., 2002. Uncertainty propagation in wildland fire behaviour modeling. *International Journal of Geographical Information Science*, 16 (2), 115–127.

Benediktsson, J. A., Swain, P. H., 1992. Consensus theoretic classification methods. *IEEE Transactions on Systems, Man, and Cybernetics*, 22 (4), 688 – 704.

Bertero, M., Boccacci, P., 1998. *Introduction to Inverse Problems in Imaging*. Institute of Physics Publishing, Bristol.

Bordley, R., 1982. A multiplicative formula for aggregating probability assessments. *Management Science*, 28 (10), 1137–1148.

Caers, J., Hoffman, T., 2006. The probability perturbation method: A new look at Bayesian inverse modeling. *Mathematical Geology* (in press).

Carle, S. F., Fogg, G. E., 1996. Transition probability-based indicator geostatistics. *Mathematical Geology*, 28 (4), 453 – 476.

Crosetto, M., Ruiz, J. A. M., Crippa, B., 2001. Uncertainty propagation in models driven by remotely sensed data. *Remote Sensing of Environment*, 76 (3), 373 – 385.

Gonzalez, R. C., Woods, R. E., 2002. *Digital Image Processing*. Prentice Hall, New Jersey.

Goovaerts, P., 1997. *Geostatistics for Natural Resources Evaluation*. Oxford University Press, New York.

Journel, A. G., 1983. Nonparametric-estimation of spatial distributions. *Mathematical Geology*, 15 (3), 445 – 468.

Journel, A. G., 2002. Combining knowledge from diverse sources: An alternative to traditional data independence hypotheses. *Mathematical Geology*, 34 (5), 573 – 596.

Journel, A. G., Alabert, F., 1989. Non-gaussian data expansion in the earth sciences. *Terra Nova*, 1 (2), 123–134.

Journel, A. G., Huijbregts, C. J., 1978. *Mining Geostatistics*. Academic Press, San Diego.

Jupp, D. L. B., Strahler, A. H., Woodcock, C. E., 1988. Auto-correlation and regularization in digital images. I. Basic theory. *IEEE transactions on Geoscience and Remote Sensing*, 26 (4), 463 – 473.

Kaipio, J., Somersalo, E., 2004. *Statistical and Computational Inverse Problems*. Spinger-Verlag, New York.

Kasetkasem, T., Arora, M., Varshney, P., 2005. Super-resolution land cover mapping using a Markov random field approach. *Remote Sensing of Environment*, 96 (3-4), 302 – 314.

Kyriakidis, P. C., Dungan, J. L. 2001. A geostatistical approach for mapping thematic classification accuracy and evaluating the impact of inaccurate spatial data on ecological model predictions. *Environmental and Ecological Statistics*, 8(4), 311 – 330.

Kyriakidis, P. C., Yoo, E.-H. 2005. Geostatistical prediction and simulation of point values from areal data. *Geographical Analysis*, 37(2), 124 – 151.

Makido, Y., Shortridge, A., 2005. Land cover mapping at sub-pixel scales: Unraveling the mixed pixel. In: *Proceedings of the 8th International Conference on Geocomputation*, University of Michigan, Ann Arbor, Michigan, August 1-3, 2005.

Mao, S., Journel, A., 1998. Conditional 3D simulation of lithofacies with 2D seismic data. *Stanford Center for Reservoir Forecasting Technical Report*, Stanford University, Stanford, California.

Menke, W., 1989. *Geophysical Data Analysis: Discrete Inverse Theory*, Revised Edition. Academic Press, San Diego.

Mertens, K. C., Verbeke, L. P. C., Ducheyne, E. I., Wulf, R. R. D., 2003. Using genetic algorithms in sub-pixel mapping. *International Journal of Remote Sensing*, 24 (21), 4241 – 4247.

Mertens, K. C., Verbeke, L. P. C., Westra, T., Wulf, R. R. D., 2004. Sub-pixel mapping and sub-pixel sharpening using neural network predicted wavelet coefficients. *Remote Sensing of Environment*, 91 (2), 225 – 236.

Mosegaard, K., Tarantola, A. 1995. Monte Carlo sampling of solutions to inverse problems. *Journal of Geophysical Research*, 100(B7), 12,431 – 12,447.

Remy, N., 2004. The Stanford geostatistical earth modeling software (SGEMS): A tool for new algorithm development. In: *Proceedings of 7th International Geostatistical Congress*, Banff, Alberta, Canada, September 26 - October 1, 2004.

Richards, J. A., Jia, X., 1999. *Remote Sensing Digital Image Analysis*, 3rd Edition. Springer-Verlag, Berlin.

Sambridge, M., Mosegaard, K., 2002. Monte Carlo methods in geophysical inverse problems. *Reviews of Geophysics*, September 2002, 40(3), (3-1) – (3-29).

Seto, K., Woodcock, C., Song, C., Huang, X., LU, J., Kaufmann, R., 2002. Monitoring land-use change in the pearl river delta using landsat TM. *International Journal of Remote Sensing*, 23 (10), 1985–2004.

Strebelle, S., 2002. Conditional simulation of complex geological structures using multiple-point statistics. *Mathematical Geology*, 34 (1), 1–21.

Tarantola, A., 2005. *Inverse Problem Theory and Methods for Model Parameter Estimation*. Society for Industrial and Applied Mathematics, Philadelphia.

Tatem, A. J., Lewis, H. G., Atkinson, P. M., Nixon, M. S., 2001. Super-resolution target identification from remotely sensed images using a Hopfield neural network. *IEEE Transactions on Geoscience and Remote Sensing*, 39 (4), 781 – 96.

Tatem, A. J., Lewis, H. G., Atkinson, P. M., Nixon, M. S., 2002. Super-resolution land cover pattern prediction using a Hopfield neural network. *Remote Sensing of Environment*, 79 (1), 1 – 14.

Tatem, A. J., Lewis, H. G., Atkinson, P. M., Nixon, M. S., 2003. Increasing the spatial resolution of agricultural land cover maps using a Hopfield neural network. *International Journal of Geographical Information Science*, 17 (7), 647 – 72.

Tso, B., Mather, P., 2001. *Classification Methods for Remotely Sensed Data*. Taylor and Francis, London.

Verhoeye, J., De Wulf, R., 2001. Land cover mapping at sub-pixel scales using linear optimization techniques. *Remote Sensing of Environment*, 79 (1), 96–104.

	nugget	structure 1		structure 2	
class		sill	range	sill	range
#1	0.09	0.52	12	0.39	70
#2	0.14	0.50	7	0.36	70
#3	0.10	0.52	9	0.38	65

Table 1: Parameters of indicator variogram models for the reference land cover map of Figure 1. Both structures #1 and #2 refer to exponential variogram functions, partial sills are expressed as proportions of a unit total sill, and ranges are expressed in TM pixels.

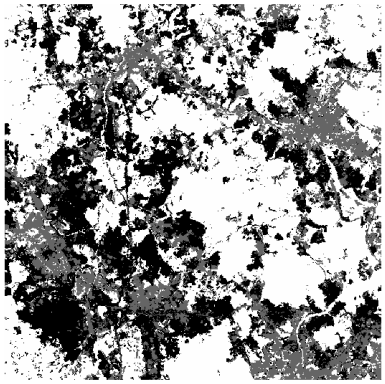

Figure 1: Reference land cover classification based on Landsat TM imagery of 500×500 pixels, each of size $30m \times 30m$. White color indicates vegetation, gray urban, black bare soil. The scene is 15km by 15km.

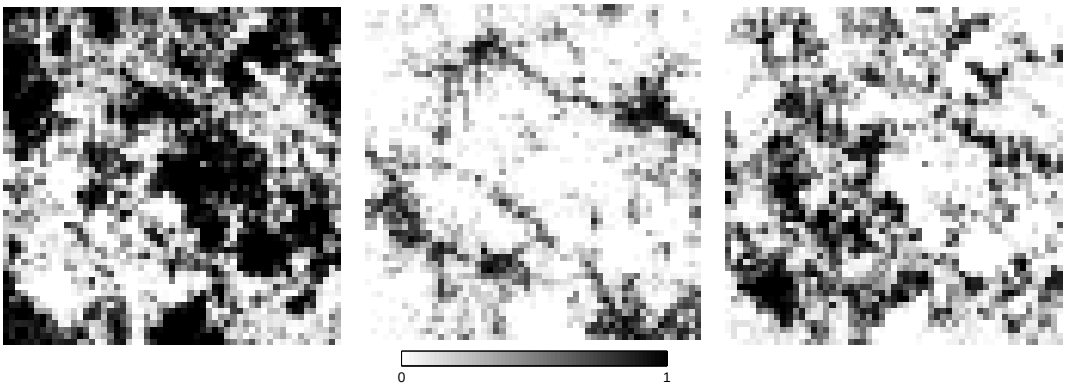

(a) Vegetation (b) Urban (c) Bare soil

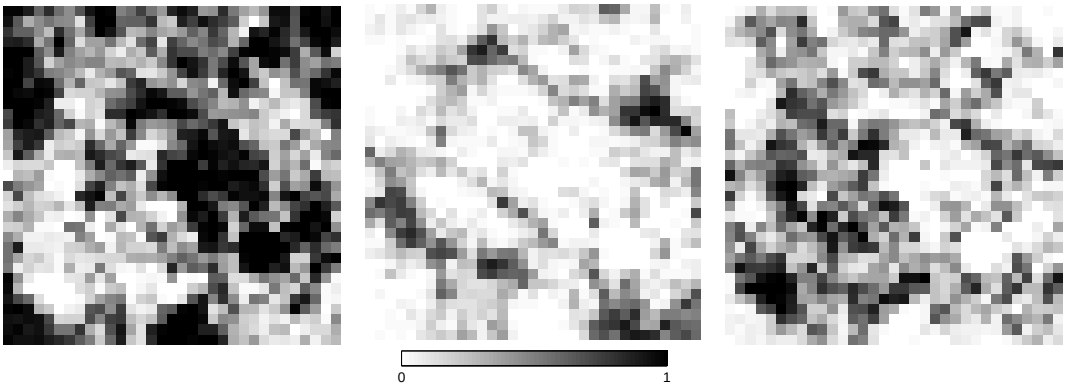

(d) Vegetation (e) Urban (f) Bare soil

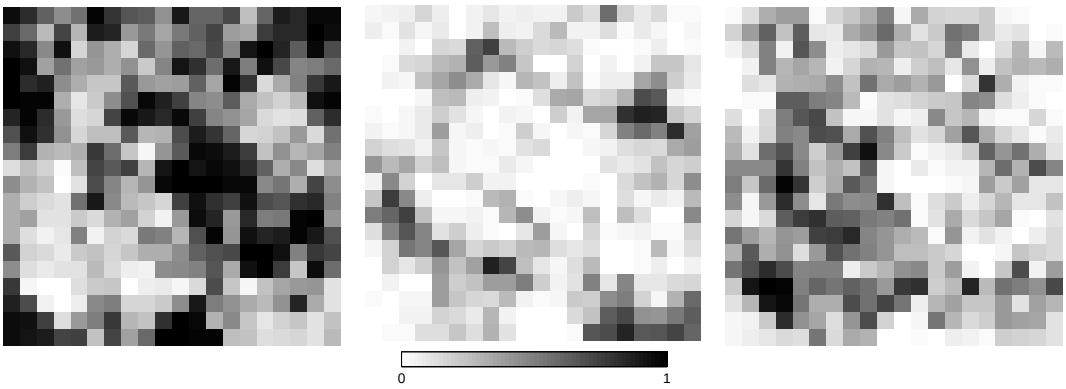

(g) Vegetation (h) Urban (i) Bare soil

Figure 2: Maps of class fractions obtained at progressively coarser spatial resolutions. The fraction value at each coarse pixel is the average of the fine resolution class indicators within that coarse pixel derived from Figure 1. **Top row:** 9×9 upscaling scheme with pixel size 270m $\times$ 270m. **Middle row:** 15×15 upscaling scheme with pixel size 450m $\times$ 450m. **Bottom row:** 25×25 upscaling scheme with pixel size $750m \times 750m$. The scene is 15km by 15km.

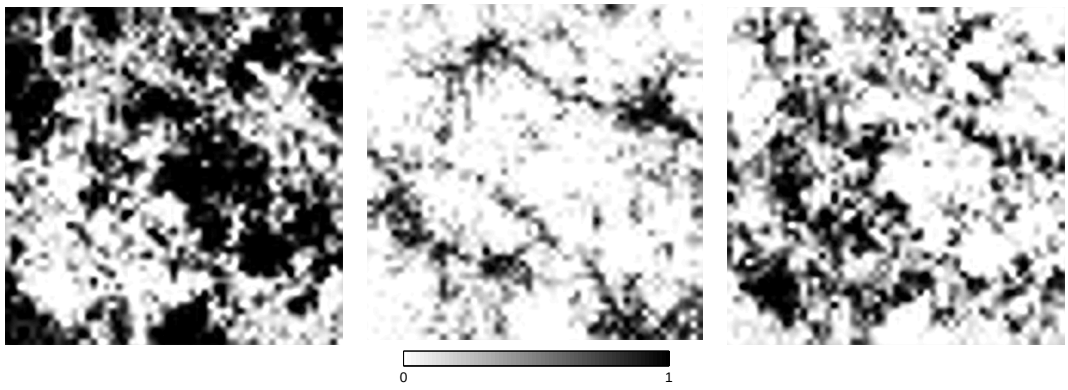

(a) Vegetation (b) Urban (c) Bare soil

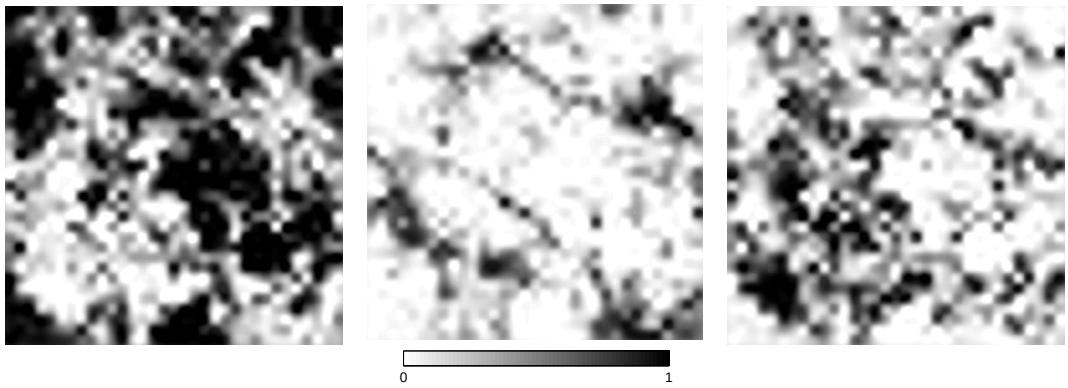

(d) Vegetation (e) Urban (f) Bare soil

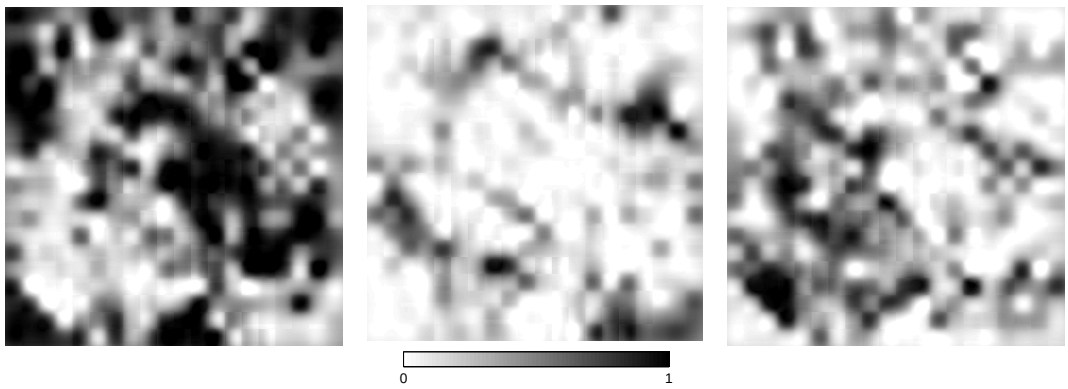

(g) Vegetation (h) Urban (i) Bare soil

Figure 3: Conditional probabilities of fine resolution class occurrence computed via simple indicator coKriging (ICK). For each row, the conditioning information consists only of the coarse resolution fractions of the corresponding row of Figure 2. **Top row:** 9×9 upscaling scheme. **Middle row:** 15×15 upscaling scheme. **Bottom row:** 25×25 upscaling scheme. The scene is 15km by 15km.

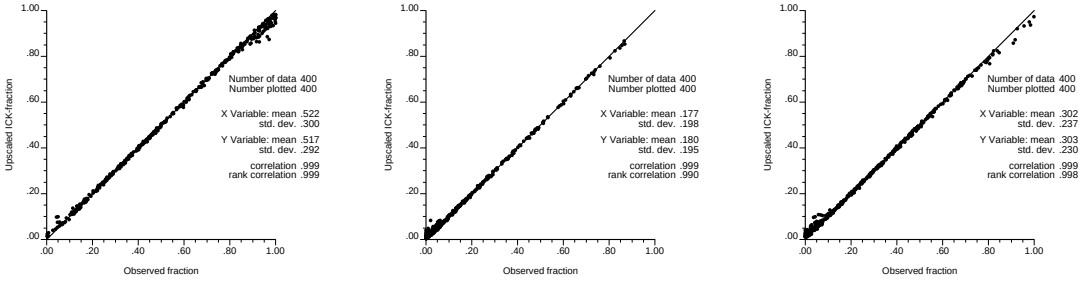

(a) Vegetation (b) Urban (c) Bare soil

Figure 4: Reproduction of coarse class fractions by the corresponding upscaled ICK-derived probabilities for the 25×25 upscaling scheme of Figure 3(g)-(i).

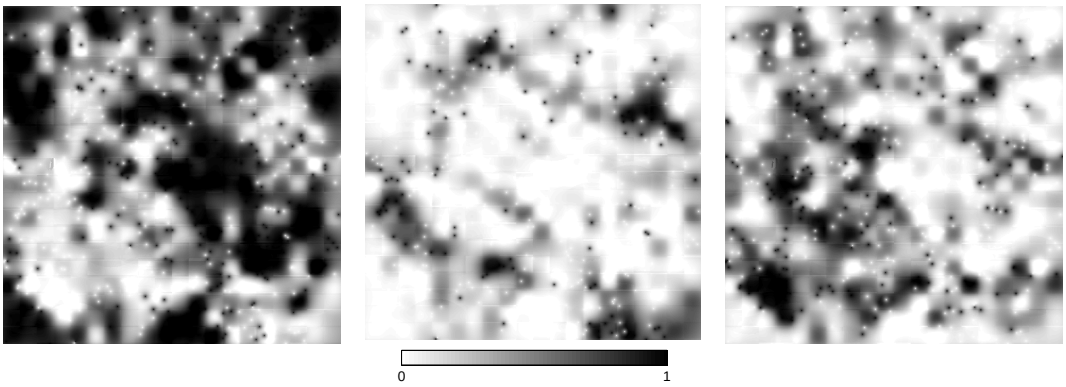

(a) Vegetation (b) Urban (c) Bare soil

Figure 5: Conditional probabilities of fine resolution class occurrence computed via simple indicator coKriging (ICK). The conditioning information consists of the coarse resolution fractions of Figure 2(g)-(i) corresponding to the 25×25 upscaling scheme, and of 500 fine resolution class labels. The scene is 15km by 15km.

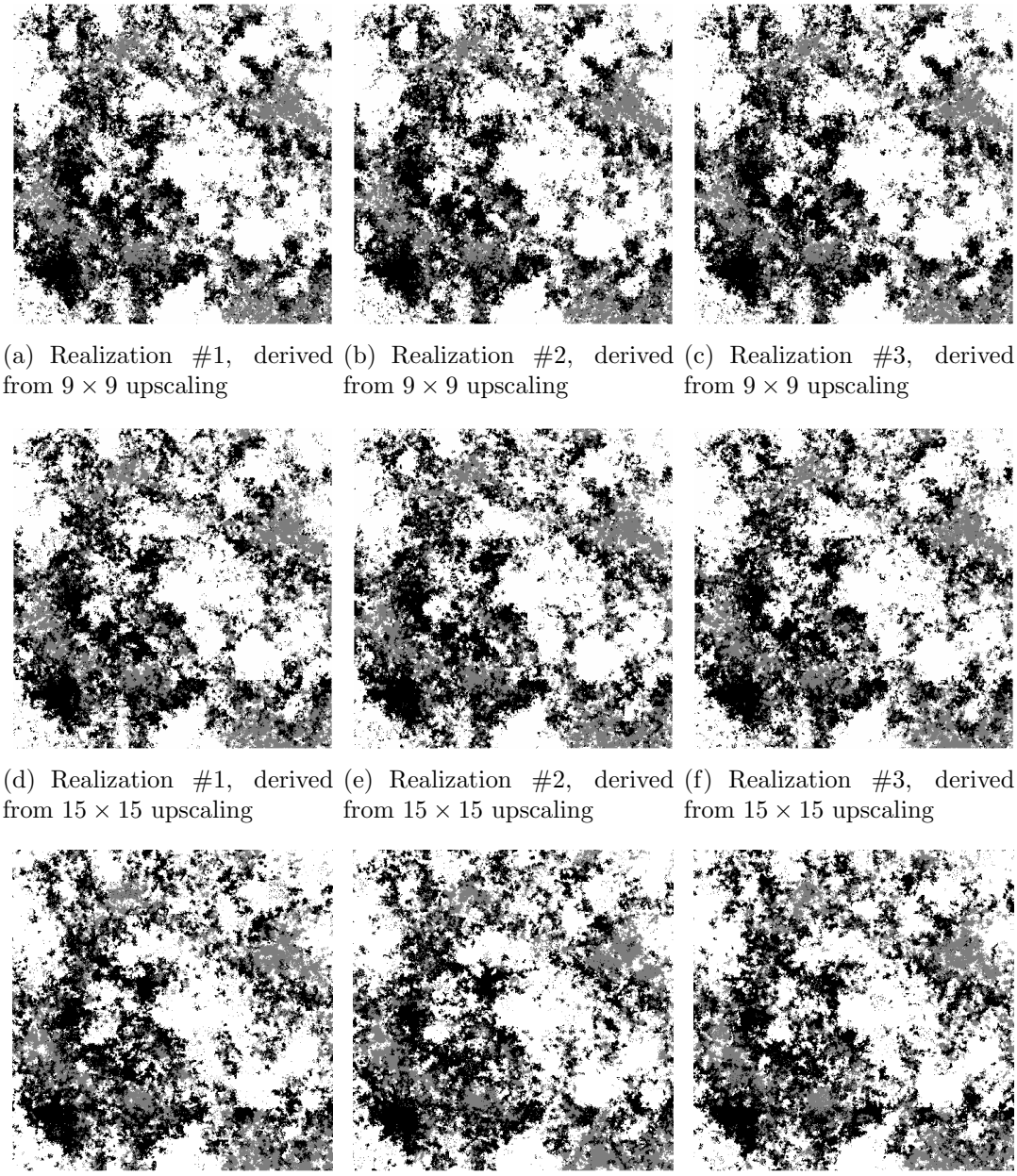

(a) Realization #1, derived from 9×9 upscaling

(b) Realization #2, derived from 9×9 upscaling

(c) Realization #3, derived from 9×9 upscaling

(d) Realization #1, derived from 15×15 upscaling

(e) Realization #2, derived from 15×15 upscaling

(f) Realization #3, derived from 15×15 upscaling

(g) Realization #1, derived from 25×25 upscaling

(h) Realization #2, derived from 25×25 upscaling

(i) Realization #3, derived from 25×25 upscaling

Figure 6: Simulated super-resolution land cover maps, generated using SIS with the progressive correction algorithm; see text for details. White color indicates vegetation, gray urban, black bare soil. For each row, the conditioning information consists only of the coarse resolution fractions of the corresponding row of Figure 2. The scene is 15km by 15km.

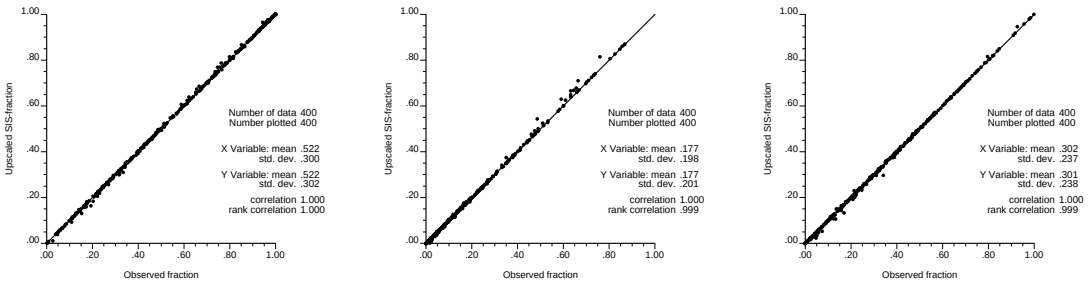

(a) Vegetation (b) Urban (c) Bare soil

Figure 7: Reproduction of the coarse class fractions for the 25×25 upscaling scheme shown in Figure 2(g)-(i) by the corresponding upscaled simulated super-resolution realizations of Figure 6(g)-(i).

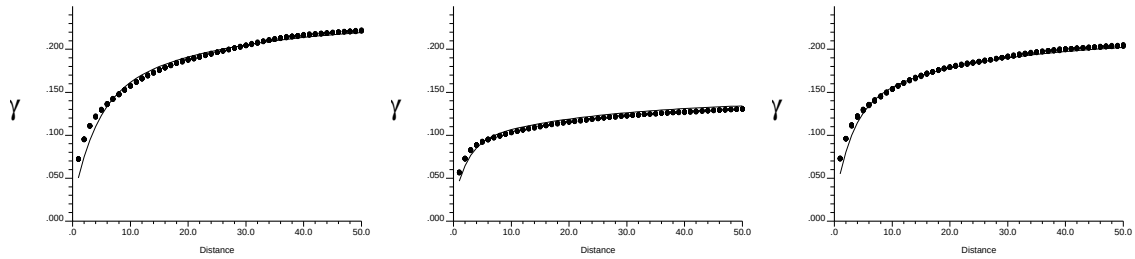

(a) Vegetation, 9×9 upscaling (b) Urban, 9×9 upscaling (c) Bare soil, 9×9 upscaling

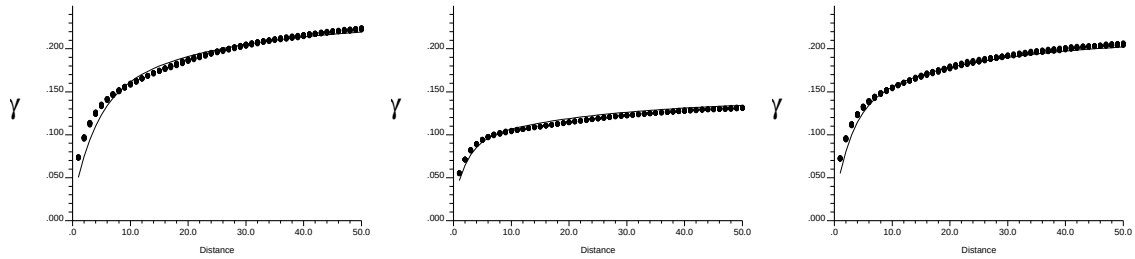

(d) Vegetation, 15×15 upscaling (e) Urban, 15×15 upscaling (f) Bare soil, 15×15 upscaling

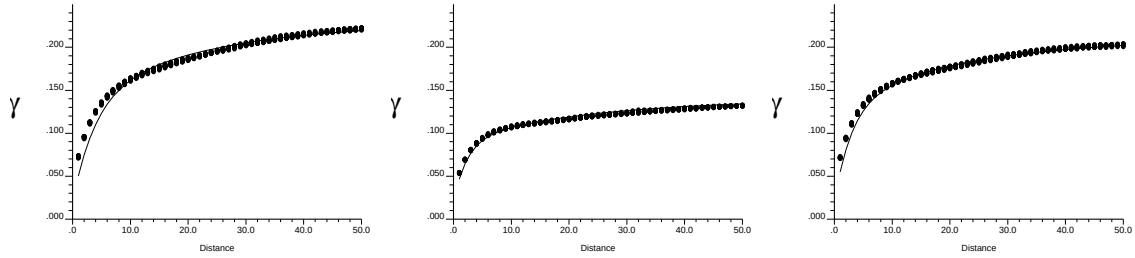

(g) Vegetation, 25×25 upscaling (h) Urban, 25×25 upscaling (i) Bare soil, 25×25 upscaling

Figure 8: Indicator variogram reproduction for 25 super-resolution realizations of land cover generated conditional to progressively coarser class fraction data; see text for details. Solid lines indicate the reference isotropic variogram models, dots correspond to variograms of simulated super-resolution land cover maps.

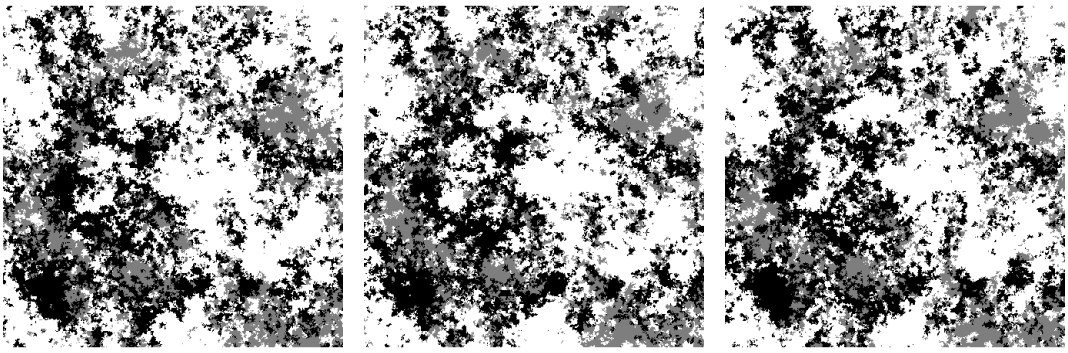

(a) Realization #1 (b) Realization #2 (c) Realization #3

Figure 9: Three super-resolution realizations of land cover generated using SIS without the progressive correction algorithm; see text for details. White color indicates vegetation, gray urban, black bare soil. The conditioning information consists of the coarse resolution fractions of Figure 2(g)-(i) corresponding to the 25×25 upscaling scheme. The scene is 15km by 15km.

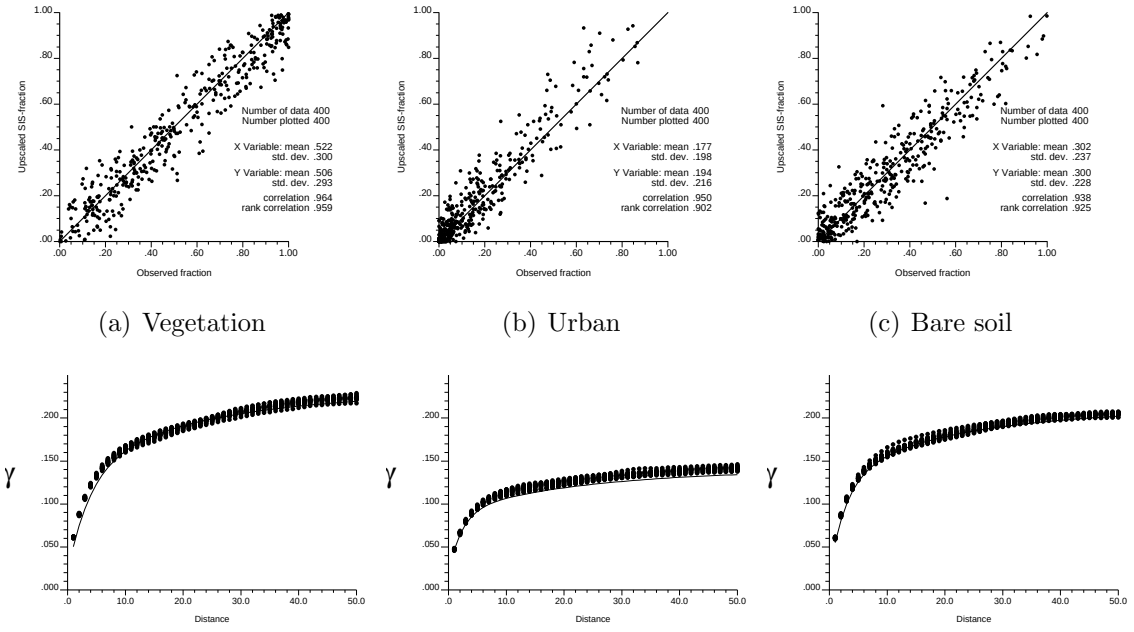

(a) Vegetation (b) Urban (c) Bare soil

(d) Vegetation (e) Urban (f) Bare soil

Figure 10: **Top row:** Reproduction of the coarse class fractions for the 25×25 upscaling scheme shown in Figure 2(g)-(i) by the upscaled simulated super-resolution realizations of Figure 9. **Bottom row:** Indicator variogram reproduction for 25 super-resolution realizations of land cover from the 25×25 upscaling scheme without the progressive correction algorithm; see text for details. Solid lines pertain to the reference isotropic indicator variogram models, whereas dots pertain to indicator variograms of simulated super-resolution land cover maps.

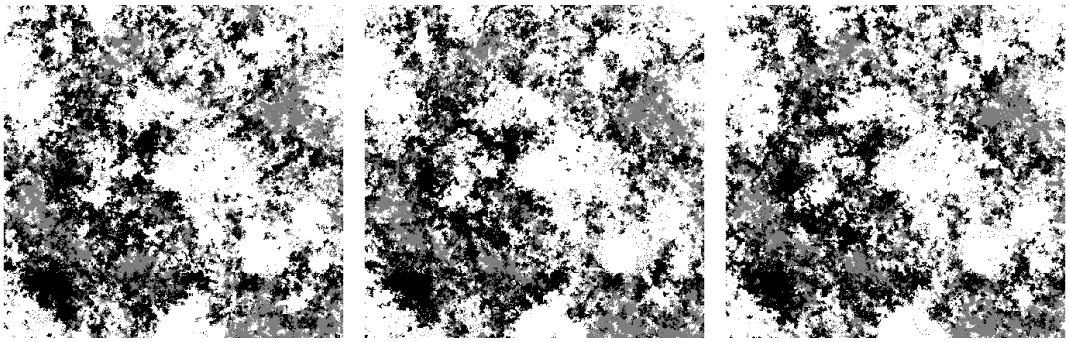

(a) Realization #1 (b) Realization #2 (c) Realization #3

Figure 11: Three super-resolution realizations of land cover conditioned to the coarse class fractions of Figure 2(g)-(i) corresponding to the 25×25 upscaling scheme, and to 500 fine resolution class labels. White color indicates vegetation, gray urban, black bare soil. The scene is 15km by 15km.

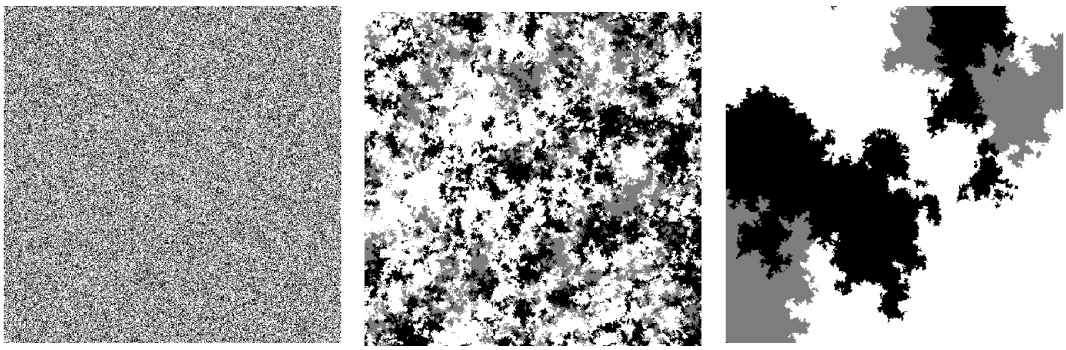

(a) Purely random; no coarse fraction data

(b) Reference variogram; no coarse fraction data

(c) Strong continuity; no coarse fraction data

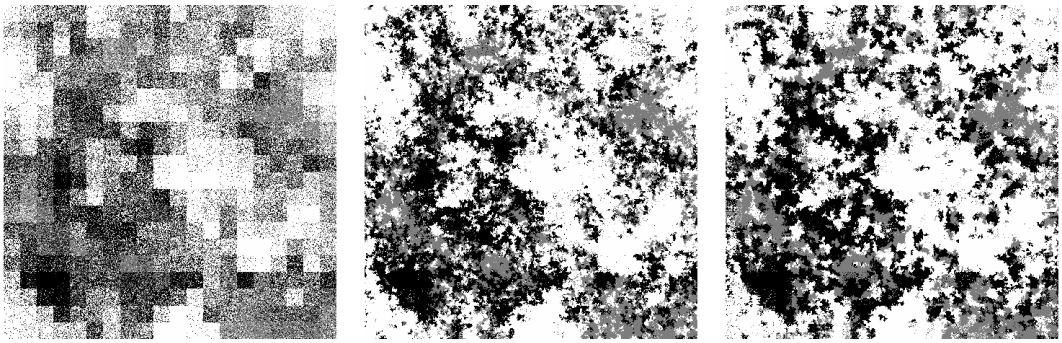

(d) Purely random

(e) Reference variogram

(f) Strong continuity

Figure 12: **Top row:** Three unconditional super-resolution realizations of land cover, generated using different indicator variogram models; see text for details. **Bottom row:** Three super-resolution realizations of land cover conditioned to the coarse fractions of Figure 2(g)-(i) corresponding to the 25×25 upscaling scheme, generated using the same indicator variogram models used for Figure 12(a)-(c); see text for details. White color indicates vegetation, gray urban, black bare soil. The scene is 15km by 15km.

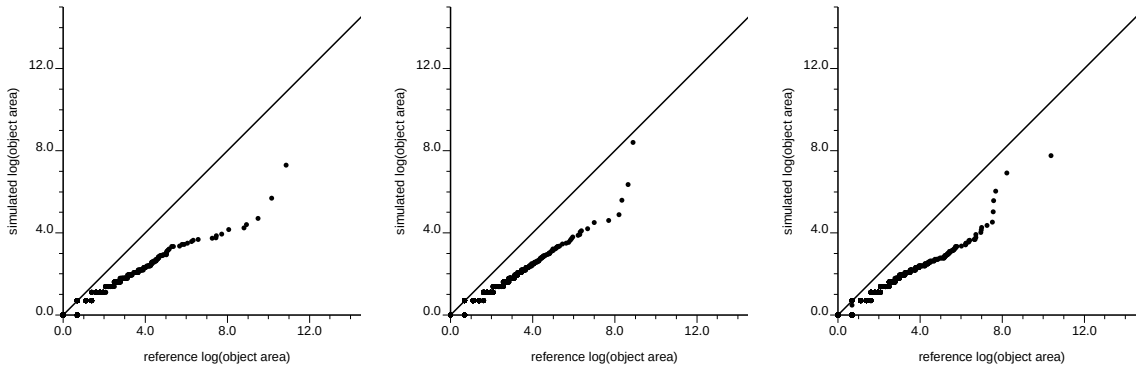

(a) Vegetation (b) Urban (c) Bare soil

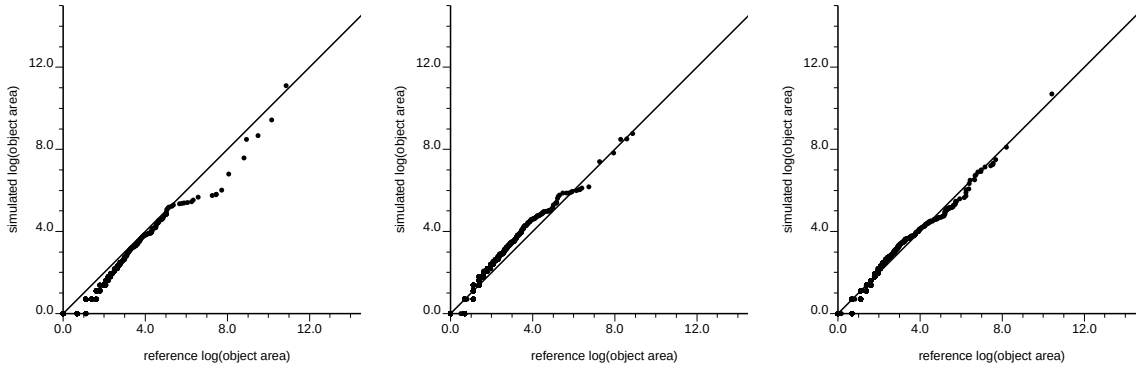

(d) Vegetation (e) Urban (f) Bare soil

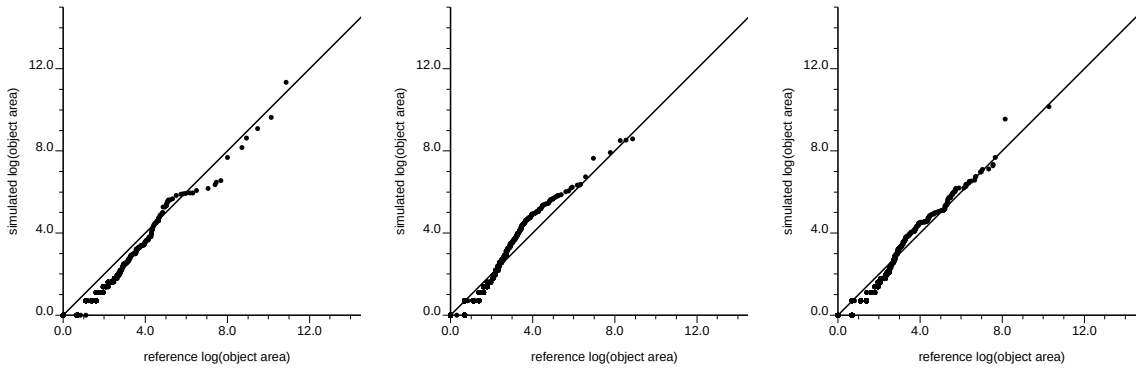

(g) Vegetation (h) Urban (i) Bare soil

Figure 13: Quantile-quantile plots between distributions of object areas derived from the reference land cover map of Figure 1 for each class, and the super-resolution realizations of: Figure 12(d) – **top row**, Figure 12(e) – **middle row**, and Figure 12(f) – **bottom row**; see text for details. All distributions pertain to the natural logarithm of area values.